



Convective Drying Analysis of Transversely Isotropic Natural Clay

Mohammadreza Mir Tamizdoust, Ph.D., A.M.ASCE¹; and Omid Ghasemi-Fare, Ph.D., A.M.ASCE²

Abstract: The drying phenomenon in clays is a multiphysical process accompanied by alterations in the thermal, hydraulic, and mechanical states of the multiphase system. Reversible and irreversible characteristics of shrinkage deformation have been observed experimentally in clayey soils for different ranges of moisture contents. The kinematics of drying due to evaporation and drying-induced shrinkage can be studied by utilizing a coupled thermo-hydro-mechanical (THM) model. An accurate evaluation of drying-induced shrinkage is needed to investigate the thermal cracking and damage of geomaterials. In this study, we developed a thermoporoelastoplastic constitutive framework assuming a non-associative plastic flow rule that can accurately model the transversely isotropic behavior of stiff natural clays in unsaturated conditions. All material parameters used in the non-associative transversely isotropic constitutive model were calibrated based on experimental observations of Boom clay. Then, the capability of the model was assessed by analyzing the convective drying experiment on natural Boom clay. The comparison of the numerical and experimental results confirms the plausibility of the hypotheses made in this study. The results show that the first stage of evaporation ends rapidly and the falling rate period (second stage of evaporation) is the dominant evaporation mechanism due to the intrinsic hydraulic properties of Boom clay and the high evaporative demand of the environment. The developed model reasonably captures the anisotropic elastic and plastic deformations of the clayey soil during the transient drying process. Numerical results demonstrate that drying shrinkage induces a 30% reduction in porosity in which approximately 82% of the total volumetric deformation in drying-induced shrinkage is irrecoverable (i.e., plastic). Moreover, the results indicate that most of the plastic deformation occurs in the first couple of hours of the drying process, when the soil's unsaturated condition is in a funicular state (i.e., where capillary pressure is dominant). Finally, the last section of this paper is devoted to a sensitivity analysis of the THM behavior of Boom clay with respect to its elastic and plastic strength. The parametric study shows approximately 10% more reduction in the final surface shrinkage when the difference between the slopes of the drying-induced compression line and the swelling line (i.e., $\lambda - \kappa$) is doubled. **DOI: 10.1061/(ASCE)GT.1943-5606.0002868.** © 2022 American Society of Civil Engineers.

Author keywords: Drying-induced shrinkage; Multiphase flow; Anisotropic deformation; Constitutive modeling.

Introduction

The analysis of non-isothermal multiphase flow in unsaturated soils is paramount, as it underpins different geotechnical problems, such as energy geo-structures and deep geological waste repositories. Thermo-hydro-mechanical (THM) or thermo-hydro-chemo-mechanical (THCM) approaches are frequently adopted to model non-isothermal multiphase flow in low permeable soils (e.g., clay) (Jaradat and Abdelaziz 2020; Mohajerani et al. 2012; Rutqvist et al. 2001; Sánchez et al. 2012; Tamizdoust and Ghasemi-Fare 2020a, b; Tsang et al. 2012; Wang and Fox 2020; Yu et al. 2018). In these approaches, the coupling effects of heat and mass (i.e., fluid) transfer in soil and deformation of the solid skeleton are taken into consideration. In the field of geohydrology and environmental sciences (e.g., analysis of land-atmosphere interactions and evaporation from bare soils), the mechanical response is often neglected

and only heat and mass transfer due to evaporation are studied theoretically through a coupled thermohydraulic analysis considering non-deformability of the soil (Ghasemi-Fare and Basu 2019; Novak 2010; Saito et al. 2006; Tamizdoust and Ghasemi-Fare 2020c, 2022; Wilson et al. 1997, 1994). However, when saturated or partially saturated fine-grained soils are subjected to a high suction (e.g., at its surface boundary), they begin to desaturate, which consequently leads to the shrinkage of the material. In other words, the gradient between the relative humidity (and/or temperature) of the environment and soil drives the drying (dehydration) process, where liquid within the soil evaporates and migrates to the evaporative boundary (Bittelli et al. 2008; Gerard et al. 2010; Tamizdoust et al. 2020). This process may induce a non-uniform moisture variation in the soil that can lead to drying-induced shrinkage and, consequently, desiccation cracks (Peron et al. 2013). This phenomenon is of considerable concern in geotechnical infrastructures, as it endangers the integrity of the structure by generating differential settlements and damages to road embankments, landfill covers, and engineered clay barriers for nuclear waste repositories. Given the importance of this problem in geotechnical engineering, dryinginduced shrinkage has been the subject of many theoretical and experimental studies (Ghorbani et al. 2009; Hedan et al. 2012; Ng and Leung 2012; Sánchez et al. 2014; Vesga 2008; Zamanian 2016; Zamanian et al. 2020). It has been observed experimentally that the cracks appear at the beginning of the desaturation process (where the degree of saturation is above 95% and around air-entry suction value) (Peron et al. 2009; Prime et al. 2015). In this stage, large irrecoverable deformations occur. Mechanical boundaries

¹Geotechnical Engineer, Dept. of Forensic Engineering, Bryant Consultants Operating LLC, 3360 Wiley Post Rd. #100, Carrollton, TX 75006. Email: ktamizdoust@geoneering.com

²Associate Professor, Dept. of Civil and Environmental Engineering, Univ. of Louisville, 132 Eastern Pkwy., Louisville, KY 40292 (corresponding author). ORCID: https://orcid.org/0000-0002-6804-2560. Email: omid.ghasemifare@louisville.edu

Note. This manuscript was submitted on October 20, 2020; approved on May 12, 2022; published online on July 19, 2022. Discussion period open until December 19, 2022; separate discussions must be submitted for individual papers. This paper is part of the *Journal of Geotechnical and Geoenvironmental Engineering*, © ASCE, ISSN 1090-0241.

and/or development of a moisture gradient (which leads to a suction gradient through soil-water retention) in soils are found to be the main causes of crack initiation in the drying process through increasing tensile or shear stresses.

To the authors' knowledge, there have been only a few studies that dealt with convective drying of transversely isotropic natural clays in a fully coupled THM framework. It has been shown in previous studies that the eye-shaped excavation damage zone (EDZ), in which the host rock may experience drying shrinkage during excavation and ventilation of an underground gallery, is clearly affected by the anisotropy of the materials (François et al. 2014; Guayacan-Carrillo et al. 2017). Further, shrinkage of transversely isotropic natural clays during the drying process is typically assumed to be thermoporoelastic, such that any plastic deformation is disregarded (Hubert et al. 2018). However, evaluation of plastic and elastic deformation during a transient state of drying is important to account for ductile-brittle transition in drying clays, especially Boom clay, which is the subject of the current study (Le Pense et al. 2016).

In this research, the unsaturated anisotropic thermoporoelastoplastic constitutive model is presented based on the Bishop's stress (average skeleton stress) variable and the fourth-order projection tensor approach. We extend the transversely isotropic modified Cam-Clay (MCC) model originally proposed by Semnani et al. (2016) for saturated rocks to unsaturated natural clays by incorporating the non-associative plastic flow rule and considering the dependency of preconsolidation pressure on the degree of saturation. Our motivation to develop a non-associative transversely isotropic thermo-elastoplastic constitutive model is based on the experimental observations on natural Boom clay presented in Sultan et al. (2010) and Lima (2011). We focus on an initially saturated Boom clay that undergoes convective drying while no external total stress is applied. A non-isothermal multiphase framework is outlined and developed based on the thermal and chemical equilibrium approaches. The developed constitutive model is implemented in a fully coupled THM finite element model to study the clay's drying behavior. The numerical model is compared to and validated with the experimental observations. The current model can be used to simulate the EDZ, and analyze the swelling behavior of low to moderate natural plastic clays and/or model wetting and drying cycles in clayey soils (THM behavior of deformable soil) under different climatic conditions.

Background of the Non-Isothermal Multiphase Flow in Deformable Soils

During evaporation from the soil-atmosphere interface, two stages of evaporation are recognized experimentally (Or et al. 2013). Stage 1 is accompanied by a high rate of evaporation, when the soil is fully saturated or close to a saturated condition, and is controlled by the atmospheric evaporative demand because the water availability in the porous medium is not a limiting factor for the evaporation process (Brutsaert 2015). Stage 2 begins as the soil close to the evaporative boundary dries out. In this stage, the water availability in the drying zone cannot meet the atmospheric evaporative demand; therefore, the evaporation is controlled by the hydraulic properties of the soil, in which the drying rate decreases remarkably. The significant observation during Stage 2 of evaporation is the formation of the drying front below the evaporative boundary, which recedes deeper in the soil as the drying of the soil continues. Above the drying front, the fluid is transferred mostly in vapor diffusion form, while below the drying front, fluid is mainly delivered by capillary pressure to the drying front (Shokri et al. 2009). Moreover, it was observed in experimental research that even under isothermal conditions, evaporation from bare soils can trigger heat transfer between the soil and its surrounding environment until a thermal equilibrium condition is reached (Grzegorz and Jacek 2007). In one of the early studies, Philip and De Vries (1957) proposed the first theoretical framework and suggested a model (now known as PdV) to analyze heat, liquid, and vapor flow in soils. The PdV model has been extensively used in numerical modeling. However, in recent years the validity of some of the assumptions made in the PdV model has been questioned, such as thermally driven enhancement of vapor diffusion (Shokri et al. 2009) and equilibrium phase change assumptions in sandy soils (Smits et al. 2011; Trautz et al. 2015).

In the aforementioned areas, much attention has been given to heat and mass flow in granular soils, where subsequent deformations have been neglected (Cherati and Ghasemi-Fare 2019). As discussed before, in fine-grained soils such as clays, evaporation not only leads to volumetric shrinkage of the soil, it may also induce desiccation cracks through an increase in unbalanced suction stress (Musielak and Mierzwa 2009). It has been shown that the interaction between fluid phases (liquid and gas) and solid phase (porous matrix) is significant during the drying process in clayey soils, and the coupling parameters play crucial roles to accurately model this phenomenon. Moreover, as drying and shrinkage of soils are not equilibrated and homogeneous responses, it has been suggested that experimental and theoretical analysis should be performed in a transient state to fully capture drying kinetics (Prime et al. 2015). Fig. 1 schematically illustrates the major components of the evaporation process, such as heat exchange between the soil and the atmosphere, as well as shrinkage and dissociation cracks at a large scale (field-scale) and the two stages of evaporation at a representative elementary volume (REV) scale.

In general, volume reduction in fully and partially saturated soils is caused by the external load (e.g., external stress) when it is transferred to the solid skeleton, and increases the effective stress. Furthermore, suction stress due to environmental evaporative demand can also increase the interparticle effective stress (Dong et al. 2020). Thus, in a case where there is no external loading (no changes in total stress), the total suction stress is the sole parameter that alters the effective stress and can provoke changes in soil stiffness and causes deformation. Conventional geotechnical laboratory tests on natural and compacted fine-grained soils denote that, in the case of drying, clayey soils undergo volume reduction; on the other hand, during wetting, they experience expansion (swelling) (Alonso et al. 2005; Coccia and McCartney 2016; Romero et al. 2011; Viola et al. 2005). Different hydro-mechanical behaviors were reported, such as swelling due to wetting (Cui et al. 2002; Villar et al. 2016), distinct macro- and microstructural deformation (Della Vecchia and Romero 2013; Joshaghani and Ghasemi-Fare 2019), and drying/wetting hydraulic hysteresis (Nuth and Laloui 2008). In addition to experimental research, many hydromechanical constitutive models have recently been proposed to account for different hydro-mechanical behaviors (Cherati and Ghasemi-Fare 2021; Vecchia and Romero 2013).

Furthermore, natural soils/rocks or compacted soils may show strong inherent fabric anisotropy, which plays an important role in their mechanical behavior and permeability (Braun et al. 2021; François et al. 2014; Li et al. 2020). Experimental models have demonstrated that sedimentary natural clay and crystalline rock have strong cross-anisotropic (or transversely isotropic) features, which are usually referred to as distinct bedding planes at the macroscale (Aliabadian et al. 2019). However, the anisotropic response of clay and rock is the consequence of multiple microstructural mechanisms that may differ for effective media of different sampling sizes (Bryant and Sun 2019). Sultan et al. (2010) showed that

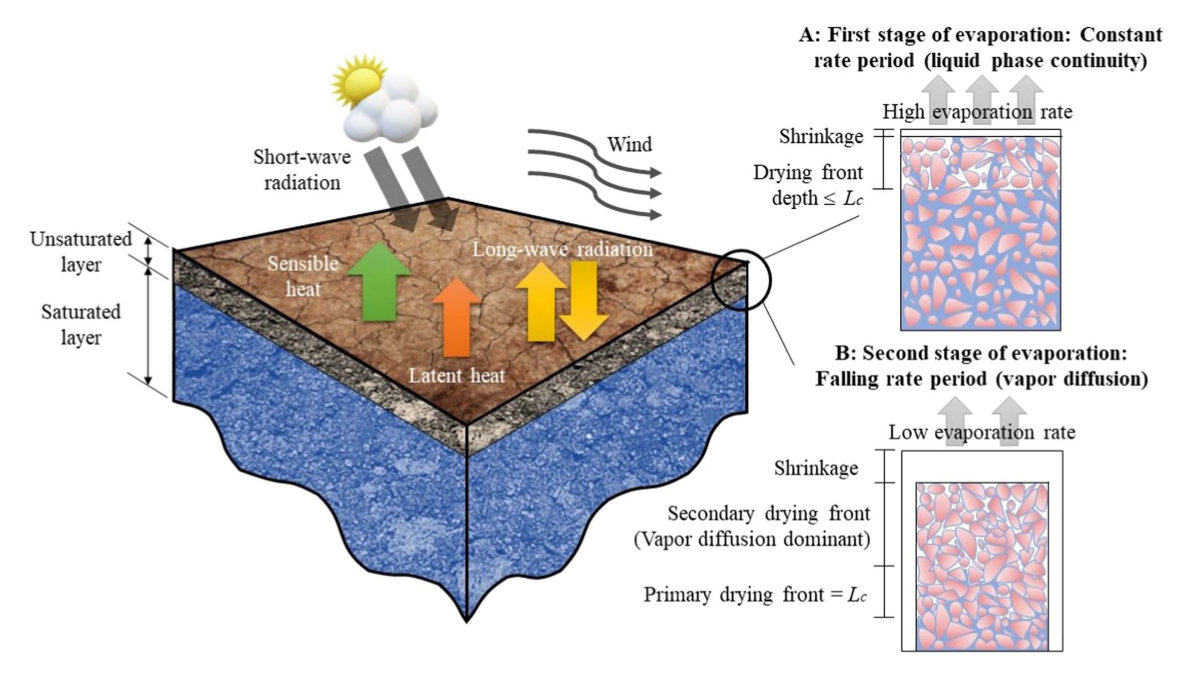


Fig. 1. Schematic illustration of heat and mass exchange across the soil-atmosphere boundary, first and second stages of evaporation, shrinkage deformation, and desiccation cracks on the soil surface through 3D large-scale and 2D representative elementary volume.

an inherent anisotropy of saturated natural Boom clay can be erased at high external isotropic loading conditions. In contrast, Lima (2011) observed strong anisotropic deformation for a series of drying tests on unsaturated natural Boom clay at different suctions while the specimens were confined by external stress close to the in-situ condition. He observed that the effect of anisotropy did not disappear even at a suction value equal to 300 MPa. For anisotropic or transversely isotropic geomaterials, distortional effects are manifested even under isotropic loading conditions (Romero and Jommi 2008). From a theoretical point of view, the effect of transversely isotropic characteristics on elastic behavior of geomaterials is manifested by the existence of a ratio between magnitudes of the Young's (E) or shear moduli (G) along different directions or planes. Higher ratios (E_H/E_V or G_{HH}/G_{HV}) show a stronger degree of anisotropy, in which subscripts H and V, respectively, denote horizontal and vertical directions in a triaxial space (Gao et al. 2017; Guayacan-Carrillo et al. 2017; Lings et al. 2000). Further, anisotropic plastic deformation stems from the properties of the materials and is incorporated by utilizing mixed rotational-isotropic strainhardening models (Amorosi et al. 2021; Dafalias et al. 2006; Venda Oliveira and Lemos 2014). In recent studies, anisotropic mixed strain-hardening elasto-plastic constitutive models have been extended to unsaturated soils (Chen et al. 2020; Della Vecchia and Romero 2013; Sitarenios and Kavvadas 2020). There are other approaches to incorporating anisotropy in classical isotropic models (e.g., MCC), such as employing a fourth-order projection tensor to map yield stresses into the modified stress space, which consequently results in distorted and rotated yield surface in the reference stress space (Nova 1980; Zhao et al. 2018). Semnani et al. (2016) reported that the fourth-order projection tensor can be obtained by a second-order microstructural tensor where its eigenvectors define the orientation of the axes of material symmetry. They investigated thermal effects on the strain localization in transversely isotropic rocks by incorporating anisotropic MCC and assuming an associative plastic flow rule.

Based on the foregoing discussion, the following sections, balance equations, and related constitutive models are fully elaborated

and then incorporated into the finite element numerical framework to simulate the thermo-hydro-mechanical process of clays under a fast-drying procedure.

Theoretical Formulation

In this study, the non-isothermal multiphase flow consists of liquid advection, gas diffusion, and heat flow in diffusion form at the macroscale. Gas is a mixture of water vapor and dry air, and fluid includes both liquid and gas, where the dissolved gas in the liquid is disregarded. Gas pressure is constant throughout this study and is equal to atmospheric pressure (100 kPa). Moreover, the phase change is at the equilibrium (i.e., instantaneous phase change) and only occurs between liquid water and water vapor (i.e., evaporation/condensation). Local thermal equilibrium is assumed between all phases, which means that the same temperature is assumed at a single point for all phases. From a mechanical point of view, the soil's structure is composed of incompressible solid grains with connected pores (no occluded porosity). Furthermore, a small deformation regime is assumed, and the compression stresses are positive as is often assumed in soil mechanics. General notations and symbols are as follows:

Second- and fourth-order identity tensors are represented by the symbols 1 and \mathbb{I} , respectively. If \mathbf{A} and \mathbf{B} are arbitrary second-order tensors, then single and double contractions are defined as $\mathbf{A} \cdot \mathbf{B} = A_{ij}B_{jk}$ and $\mathbf{A}:\mathbf{B} = A_{ij}B_{ij}$, respectively. The tensorial operators used in this study are $(\mathbf{A} \otimes \mathbf{B})_{ijkl} = A_{ij}B_{kl}$; $(\mathbf{A} \oplus \mathbf{B})_{ijkl} = A_{jl}B_{jk}$; and $(\mathbf{A} \ominus \mathbf{B})_{ijkl} = A_{il}B_{jk}$. The second-order symmetric Cauchy stress tensor is composed of spherical and deviatoric parts: $\mathbf{\sigma} = [\text{tr}(\mathbf{\sigma})/3]\mathbf{1} + \mathbf{S}$, where \mathbf{S} is the deviatoric stress. Mean and deviatoric stress invariants are defined as: $p = \text{tr}(\mathbf{\sigma})/3$, and $q = \sqrt{(3/2)\mathbf{S}:\mathbf{S}}$, respectively. Following the definition of the Cauchy stress tensor, the second-order symmetric strain tensor can be expressed as $\mathbf{\varepsilon} = [\text{tr}(\mathbf{\varepsilon})/3]\mathbf{1} + \mathbf{\varepsilon}'$, where $\mathbf{\varepsilon}'$ is the deviatoric strain. Volumetric and deviatoric strain invariants are $\varepsilon_v = \text{tr}(\mathbf{\varepsilon})$, and $\varepsilon_d = \sqrt{(2/3)\mathbf{\varepsilon}':\mathbf{\varepsilon}'}$, respectively. In the following sections, all equations are presented in general multiaxial stress space.

Macroscopic Balance Equations

The mass balances of solid, water, and gas phases are presented in Eqs. (1)–(3), and the balance of energy is expressed in Eq. (4) (Coussy 2004):

Solid:
$$\frac{\partial[(1-n)\rho_s]}{\partial t} + (1-n)\rho_s \nabla \cdot v_s = 0$$
 (1)

$$\mbox{Liquid water: } \frac{\partial (nS_{w}\rho_{w})}{\partial t} + nS_{w}\rho_{w}\nabla \cdot v_{w} = -\dot{m} \eqno(2)$$

Water vapor:
$$\frac{\partial [n(1-S_w)\rho_v]}{\partial t} + \nabla \cdot (-D_v \nabla \rho_v) = \dot{m}$$
 (3)

Balance of energy:
$$(\rho C)_{eff} \frac{\partial T}{\partial t} - \lambda_{eff} \nabla^2 T = -L_v \dot{m}$$
 (4)

where n is the porosity of the medium; and S_w is the degree of saturation of water $[S_w = (1 - S_r)S_{eff} + S_r]$. S_{eff} and S_r are effective and residual degrees of saturation, respectively. S_{eff} can be determined from a soil-water retention (SWR) curve, which relates the effective degree of saturation to matric suction $(p_c \text{ [ML}^{-1}\text{T}^{-2}])$. Densities of solid grains, water, and vapor are ρ_s , ρ_w , and ρ_v (ML⁻³), respectively. v_s (LT⁻¹) is the solid velocity, and v_w (LT⁻¹) is the liquid water velocity. D_v (L²T⁻¹) is the effective diffusivity, which is defined as $D_v = n(1 - S_w)\tau D_v^0$ (where τ is tortuosity, and D_v^0 (L²T⁻¹) is the binary diffusion coefficient of vapor in the gas phase). In Eq. (3), the vapor diffusion is assumed according to Fick's first law of diffusion. \dot{m} (kg/m³/s ML⁻³T⁻¹) is denoted as the rate of phase change; the positive and negative signs indicate condensation and evaporation, respectively. In Eq. (4), $T(\Theta)$ is the temperature of the medium, C_{eff} (L² Θ^{-1} T⁻²) is the effective heat capacity, λ_{eff} (MLT⁻³ Θ^{-1}) is the effective thermal conductivity, and L_v (ML²T⁻²) is the latent heat of vaporization. In the energy balance equation heat conduction is assumed to be the sole heat transfer mechanism for the fine-grained soil.

Porosity variation can be defined through Eq. (1), and by considering incompressible solid grains (i.e., $\partial \rho_s/\partial t = 0$). Furthermore, the density of liquid water can vary with temperature and pressure (liquid water is slightly compressible). These state variables are expressed as follows:

$$\frac{\partial n}{\partial t} = (1 - n)\nabla \cdot v_{s} = (1 - n)\frac{\partial \varepsilon_{v}}{\partial t}$$
 (5)

$$\frac{\partial \rho_{w}}{\partial t} = \rho_{w} \left[c_{w} \frac{\partial p_{w}}{\partial t} - \alpha_{w} \frac{\partial T}{\partial t} \right]$$
 (6)

In Eq. (5), ε_v is the summation of the mechanical and thermal strains and can be decomposed of elastic, thermal, and plastic deformations. In Eq. (6), p_w (ML⁻¹T⁻²) indicates pore water pressure; c_w (M⁻¹LT²) is the compressibility modulus; and α_w (Θ^{-1}) is the linear thermal expansion coefficient of the water.

Equilibrium Phase Change Restriction

In general, phase change between liquid water and water vapor in a porous medium is a non-equilibrium time-dependent process and is usually adapted through the rate of phase change, \dot{m} (Niessner and Hassanizadeh 2009). In coarse-grained soil (e.g., sandy soil), the non-equilibrium approach showed promising results compared to the equilibrium phase change approach with respect to experimental observations (Tamizdoust and Ghasemi-Fare 2020c). However, in fine-grained soils (e.g., clays), phase change rapidly reaches the equilibrium state, which theoretically is interpreted to mean that the

vapor density is equal to its equilibrium value through Kelvin's equation:

$$\rho_v = \rho_{v,eq} = \rho_{v,sat}RH = \rho_{v,sat} \exp\left(-\frac{p_c M_w}{\rho_w RT}\right)$$
 (7)

where RH is the relative humidity; $\rho_{v,eq}$ and $\rho_{v,sat}$ (ML⁻³) are the equilibrium and saturated vapor densities, respectively; R = 8.3145 (Pa·m³/K/mol) is the universal gas constant; and $M_w = 0.018$ (kg/mol) is the molecular weight of water.

Mechanical Equilibrium

The mechanical equilibrium for a multiphase system is developed from the balance of linear momentum, and by assuming the quasistatic condition (Coussy 2004; Rutqvist et al. 2001):

$$\nabla \cdot \mathbf{\sigma} + [(1 - n)\rho_s + nS_w \rho_w + n(1 - S_w)\rho_v]\mathbf{g} = \mathbf{0}$$
 (8)

where \mathbf{g} (LT⁻²) is the gravitational acceleration vector; and $\boldsymbol{\sigma}$ (ML⁻¹T⁻²) is the Cauchy stress tensor. Stress and strain fields are related through the mechanical constitutive model described in the next section.

Eqs. (1)–(4) can be coupled by incorporating Eqs. (5)–(7), as follows (Rutqvist et al. 2001):

$$\begin{split} n\rho_{w}[S_{w}c_{w} + C_{p}]\frac{\partial p_{w}}{\partial t} + \nabla \cdot \left(nS_{w}\rho_{w}v_{w} - D_{v}\nabla\rho_{v,eq}\right) \\ &= \rho_{w}S_{w}\left[n\alpha_{w}\frac{\partial T}{\partial t} - (1-n)\frac{\partial\varepsilon_{v}}{\partial t}\right] \end{split} \tag{9}$$

$$(\rho C)_{eff} \frac{\partial T}{\partial t} - \lambda_{eff} \nabla^2 T$$

$$= -L_v \left\{ \frac{\partial [n(1 - S_w)\rho_{v,eq}]}{\partial t} + \nabla \cdot (-D_v \nabla \rho_{v,eq}) \right\}$$
(10)

Eq. (9) is obtained by combining Eqs. (2) and (3) and employing the definition of porosity and water density variations presented in Eqs. (5) and (6), and also equilibrium vapor density. $C_p (= \partial S_w / \partial p_w)$ (M⁻¹LT²) is the moisture capacity and can be derived from the SWR curve. Temporal variation of equilibrium vapor density was disregarded because it is negligible in comparison to temporal variation of pore water pressure. In Eq. (10), the source term of the latent heat of evaporation is assumed as the vapor transport [Eq. (3)]. Pore water pressure and temperature are calculated by coupling Eqs. (9) and (10).

Constitutive Equations

Transversely Isotropic Thermoporoelastoplastic Model

In the small deformation regime, the total strain rate can be decomposed into three components (Chaves 2013):

$$\dot{\mathbf{\varepsilon}} = \dot{\mathbf{\varepsilon}}^e + \dot{\mathbf{\varepsilon}}^t + \dot{\mathbf{\varepsilon}}^p \tag{11}$$

where $\dot{\mathbf{e}}^e$ is an elastic strain rate; $\dot{\mathbf{e}}^t$ is a thermal strain rate; and $\dot{\mathbf{e}}^p$ is a plastic strain rate. The elastic, thermal, and plastic strain rates are defined as (Chaves 2013)

$$\dot{\mathbf{\epsilon}}^e = \mathbb{C}^e : \dot{\mathbf{\sigma}}' \tag{12}$$

$$\dot{\mathbf{\varepsilon}}^t = \mathbf{\alpha}_d \dot{T} \tag{13}$$

$$\dot{\boldsymbol{\varepsilon}}^p = \dot{\lambda}_p \frac{\partial g}{\partial \dot{\boldsymbol{\sigma}}'} \tag{14}$$

where σ' (ML⁻¹T⁻²) is a stress variable in a multiphase system that acts on a solid skeleton. \mathbb{C}^e (ML⁻¹T⁻²) is the elastic compliance fourth-order tensor, which is the inverse of the elastic tangent tensor: $\mathbb{C}^e = (\mathbb{D}^e)^{-1}$. Moreover, $\alpha_d (\Theta^{-1})$ is the drained linear thermal expansion coefficient tensor of the porous medium and can be expressed as $\alpha_d = \alpha_d \mathbf{1}$, assuming an isotropic thermal expansion coefficient. In Eq. (14), g (ML⁻¹T⁻²) is the plastic potential function, the gradient of which with respect to the stress variable gives the direction of the plastic strain rate. $\lambda_p \geq 0$ is the plastic multiplier and is determined from Prager's consistency condition: $f(\sigma, h(\epsilon^p)) = 0$ where f is the yield function, and h is the hardening parameter.

In the current mechanical constitutive framework, the stress variable is defined according to the average skeleton stress, which is an extension of Bishop's stress variable (Bishop 1959; Jommi 2000; Wheeler et al. 2003):

$$\mathbf{\sigma}' = \mathbf{\sigma} - [(1 - S_w)p_a + S_w p_w]\mathbf{1} \tag{15}$$

In Eq. (15), the hydro-mechanical coupling is evident from the fact that the average stress variable (σ') depends on the degree of saturation. For the fully saturated condition ($S_w = 1$), the average stress equals Terzaghi's effective stress (Terzaghi 1925). Eq. (15) has been incorporated in different constitutive models for unsaturated soils and is also adopted in the developed model in this study.

For transversely isotropic elastic materials, the elastic stored energy function can be defined as (Spencer 1984)

$$W^{e} = \frac{1}{2}\lambda_{T}\operatorname{tr}(\mathbf{\varepsilon})^{2} + \mu_{T}\operatorname{tr}(\mathbf{\varepsilon}^{2}) + a(n \cdot \mathbf{\varepsilon} \cdot n)\operatorname{tr}(\mathbf{\varepsilon}) + 2(\mu_{L} - \mu_{T})n \cdot \mathbf{\varepsilon}^{2} \cdot n + \frac{1}{2}b(n \cdot \mathbf{\varepsilon} \cdot n)^{2}$$
(16)

where λ_T , μ_T , μ_L , a, and b are elastic parameters; and n is a unit vector normal to the bedding planes and is schematically illustrated in Figs. 2(a and b). A tangent elastic tensor can be obtained from the second derivative of Eq. (16) with respect to the elastic strain

$$\mathbb{D}^{e} = \frac{\partial^{2} \mathbf{W}^{e}}{\partial \mathbf{\varepsilon} \otimes \partial \mathbf{\varepsilon}} = \lambda_{T} \mathbf{1} \otimes \mathbf{1} + 2\mu_{T} \mathbb{I} + a(\mathbf{1} \otimes n \otimes n + n \otimes n \otimes \mathbf{1}) + (\mu_{L} - \mu_{T})(\mathbf{1} \oplus n \otimes n + n \otimes n \oplus \mathbf{1} + \mathbf{1} \oplus n \otimes n + n \otimes n \oplus \mathbf{1}) + b(n \otimes n \otimes n \otimes n)$$

$$(17)$$

The elastic constants in Eqs. (16) and (17) are related to Young's moduli (parallel E_{\parallel} , and perpendicular E_{\perp} , to the bedding),

Poisson's ratios (on the bedding plane $\nu_{||||}$, and perpendicular to the bedding plane, $\nu_{||\perp}$), and shear modulus perpendicular to the bedding plane, $G_{||\perp}$. The elastic tangent tensor is also defined using Poisson's ratios, Young's moduli, and shear moduli.

In this study, the transversely isotropic elastic tensor was constructed by following the approach proposed by Graham and Houlsby (1983), which reduces the elastic parameters to three variables:

$$\alpha_{e} = \sqrt{\frac{E_{\parallel}}{E_{\perp}}}, \qquad \nu_{\parallel \perp} = \frac{\nu_{\parallel \parallel \parallel}}{\alpha_{e}}, \qquad G_{\parallel \perp} = \frac{G_{\parallel \parallel \parallel}}{\alpha_{e}} = \frac{E_{\parallel}}{2\alpha_{e}(1 + \nu_{\parallel \parallel})}$$

$$\tag{18}$$

where α_e demonstrates the degree of elastic anisotropy: $\alpha_e=1$ replicates the elastic isotropic material while $\alpha_e<1$ implies that the stiffness of the material is higher in the perpendicular direction than in the direction parallel to the bedding planes, and the reverse apples for $\alpha_e>1$. Young's moduli depend on the effective stress and are defined in this study based on the expression that was originally proposed for saturated clays (Modaressi and Laloui 1997):

$$E_i = E_{i,ref} \left(\frac{p'}{p'_{ref}}\right)^{n_e}; \quad i = \| \text{ or } \bot$$
 (19)

where E_{ref} (ML⁻¹T⁻²) is a reference to Young's modulus; p' is the mean effective stress; p'_{ref} (ML⁻¹T⁻²) is the reference pressure; and n_e is a constant. Eqs. (17)–(19) are used in this work to construct the elastic tangent tensor, as discussed in the Appendix.

One of the effective approaches to extend the isotropic plasticity model to present a transversely isotropic material is to define a projection tensor that maps the Cauchy stress tensor to an alternative stress space:

$$\mathbf{\sigma}^{\prime *} = \mathbb{P} : \mathbf{\sigma}^{\prime} \tag{20}$$

where \mathbb{P} is the fourth-order symmetric projection tensor; and $\sigma^{/s}$ is the Cauchy stress tensor in alternative stress space. This constitutive approach was successfully utilized to investigate the strength and deformation of the sedimentary rocks in Zhao and Borja (2020). Semnani et al. (2016) established such a projection tensor by employing a second-order microstructure tensor, defined as

$$\mathbf{m} = n \otimes n \tag{21}$$

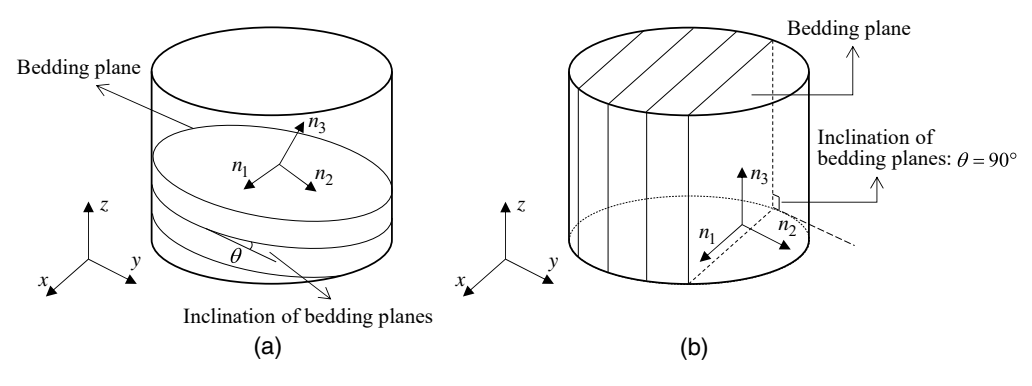


Fig. 2. Schematic representation of bedding planes and their unit normal vectors in a transversely isotropic material: (a) arbitrary direction of bedding planes; and (b) perpendicular direction of bedding planes in which the unit normal vector is aligned with the Cartesian coordinate system.

The microstructure tensor characterizes an arbitrary bedding orientation with respect to the global coordinate system. The projection tensor can be defined using Eq. (22) (Semnani et al. 2016):

$$\mathbb{P} = c_1 \mathbb{I} + \frac{c_2}{2} (\mathbf{m} \oplus \mathbf{m} + \mathbf{m} \oplus \mathbf{m})$$

$$+ \frac{c_3}{4} (\mathbf{1} \oplus \mathbf{m} + \mathbf{m} \oplus \mathbf{1} + \mathbf{1} \oplus \mathbf{m} + \mathbf{m} \oplus \mathbf{1})$$
 (22)

where c_1 , c_2 , and c_3 are material constants. In a case when the coordinate system is aligned with the bedding planes, such as is shown in Fig. 2(b), the projection tensor in Eq. (22) can be simplified as a diagonal fourth-order tensor. The projection tensor in Vogt's notation can be expressed as

$$\begin{pmatrix}
\sigma_{11}^{\prime *} \\
\sigma_{22}^{\prime *} \\
\sigma_{33}^{\prime *} \\
\sigma_{23}^{\prime *} \\
\sigma_{13}^{\prime *} \\
\sigma_{12}^{\prime *}
\end{pmatrix} =
\begin{bmatrix}
\beta & 0 & 0 & 0 & 0 & 0 \\
0 & \alpha & 0 & 0 & 0 & 0 \\
0 & 0 & \beta & 0 & 0 & 0 \\
0 & 0 & 0 & \gamma & 0 & 0 \\
0 & 0 & 0 & 0 & \beta & 0 \\
0 & 0 & 0 & 0 & 0 & \gamma
\end{bmatrix}
\begin{pmatrix}
\sigma_{11}^{\prime} \\
\sigma_{22}^{\prime} \\
\sigma_{33}^{\prime} \\
\sigma_{23}^{\prime} \\
\sigma_{13}^{\prime} \\
\sigma_{12}^{\prime}
\end{pmatrix} (23)$$

where

$$\alpha = c_1 + c_2 + c_3$$
 $\beta = c_1$
 $\gamma = c_1 + c_3/2$ (24)

It is clear that in the case of $\alpha = \beta = \gamma = 1$, alternative and actual stresses are identical ($\sigma'^* = \sigma'$). However, when the coordinate system is aligned with the bedding planes, the expression presented in Eq. (23) can be used to map the yield and plastic potential functions. To do that, one can define alternative stress invariants as functions of mapped stress ($\sigma^{\prime*}$). These functions are perceived as isotropic in the mapped stress space and anisotropic in the actual stress space. Moreover, yield and potential functions may possess different analytical forms if the non-associative plastic flow rule is supported by the experimental evidence (Dafalias et al. 2006; Veiskarami and Tamizdoust 2017). In this study, we performed the mapping procedure on the MCC, and the main equations of the non-associative thermoporoelastoplastic constitutive model for transversely isotropic natural clays are outlined subsequently. Eq. (25) demonstrates the MCC plastic potential in the mapped stress space:

$$g_{aniso} = \frac{q_g^{*2}}{p_g^{**}M_g^2} + p_g^{**} - p_\alpha = 0$$
 (25)

where the asterisk superscript refers to mapped stress invariants; the subscript g refers to the fact that mapped stress invariants are applied to the plastic potential function; M_g is the stress ratio at the critical state, in which its dependency on the Lode's angle is disregarded; and p_{α} (ML⁻¹T⁻²) is a dummy index to ensure that the analytical expression in Eq. (25) is satisfied. By considering the proposed plastic potential function, the plastic strain rate direction in Eq. (14) can be rewritten as follows:

$$\dot{\mathbf{e}}^p = \dot{\lambda}_p \frac{\partial g_{aniso}}{\partial \mathbf{\sigma}'} = \dot{\lambda}_p \mathbb{P}_g : \frac{\partial g_{iso}}{\partial \mathbf{\sigma}_s'^*}$$
 (26)

In the triaxial stress space, and by combing Eqs. (25) and (26), the stress-dilatancy relation can be obtained as

$$\psi = \frac{\dot{\varepsilon}_v^p}{\dot{\varepsilon}_d^p} = \frac{M_g^2 - \eta_g^{*2}}{2\eta_q^*}, \qquad \eta_g^* = \frac{q_g^*}{p_g^{'*}}$$
(27)

where η_g^* is the stress ratio in the mapped stress configuration. Similar to the plastic potential function, yield surface is expressed as:

$$f_{\text{aniso}} = \frac{q_f^{*2}}{p_f^{'*} M_f^2} + p_f^{'*} - p_{csT} = 0$$
 (28)

where the subscript f indicates that mapped stress invariants are applied to the yield function; and M_f is a material constant similar to M_g . Furthermore, p_{csT} (ML⁻¹T⁻²) is the preconsolidation pressure:

$$\begin{aligned} p_{csT} &= p_{c0} \left[1 - \gamma_T \log \left(\frac{T}{T_0} \right) \right] \\ &\times \left\{ 1 + b_1 (\exp[b_2 (1 - S_w)] - 1) \right\} \exp \left(\frac{\varepsilon_v^p}{\beta_p} \right) \end{aligned} \tag{29}$$

where p_{c0} (ML⁻¹T⁻²) is the initial preconsolidation pressure. The preconsolidation pressure in Eq. (29) defines the isotropic growth/ shrinkage of the yield surface with respect to the thermo-hydromechanical evolution. The first bracket on the right hand side of Eq. (29), which was proposed by Laloui and Cekerevac (2003), represents the thermal hardening/softening process, where γ_T is a material constant and T_0 is the initial temperature. The second bracket controls the drying-induced hardening with respect to changes in the degree of saturation, according to Romero and Jommi (2008), where b_1 and b_2 are the soil's constants. The last term is the isotropic strain-hardening variable, which was already incorporated in the original isotropic MCC model. $\beta_p = (\lambda - \kappa)/$ $(1 + e_0)$ is the plastic compressibility modulus; e_0 is the reference void ratio; and λ , and κ are, respectively, the parameters related to the slope of the drying-induced compression line and swelling line. The effect of suction on these parameters has been considered in constitutive models developed by Gens and Alonso (1992) and Della Vecchia et al. (2010). In this study, for simplicity λ and κ are considered as constants.

In Figs. 3(a and b), graphical representations of the mapped yield and plastic potential functions are shown in the triaxial alternative p'^*-q^* and actual p'-q stress invariants. The mapping is depicted by changing the β value while keeping $\alpha=\gamma=1$. Figs. 3(a and b) show that the mapped yield surface and plastic potential are isotropic in the p'^*-q^* stress space, while they are anisotropic in the p'-q stress space. The anisotropy of the yield and plastic potential functions in the actual stress space is different from one another, as two different projection tensors $(\mathbb{P}_f \neq \mathbb{P}_g)$ are applied to (p'_f, q_f) and (p'_g, q_g) .

Hydraulic Constitutive Model and SWR Characteristics

In this study, the unsaturated fluid flow in a transversely isotropic medium is governed by the Darcy's flow:

$$nS_w v_w = -\frac{\mathbf{\kappa}_{\text{int}} \kappa_{rw}}{\mu_w} (\nabla p_w + \rho_w g) \tag{30}$$

where μ_w (ML⁻¹T⁻¹) is the dynamic viscosity of water; κ_{rw} is the relative permeability of water; and κ_{int} (L²) is the second-order intrinsic permeability tensor of the medium, defined as

$$\mathbf{\kappa}_{\text{int}} = \kappa_{\text{int},\perp} \mathbf{m} + \kappa_{\text{int},\parallel} (\mathbf{1} - \mathbf{m}) \tag{31}$$

where $\kappa_{\text{int},\parallel}$ and $\kappa_{\text{int},\perp}$ (L²) are the intrinsic permeability components, parallel and perpendicular to the bedding planes, respectively.

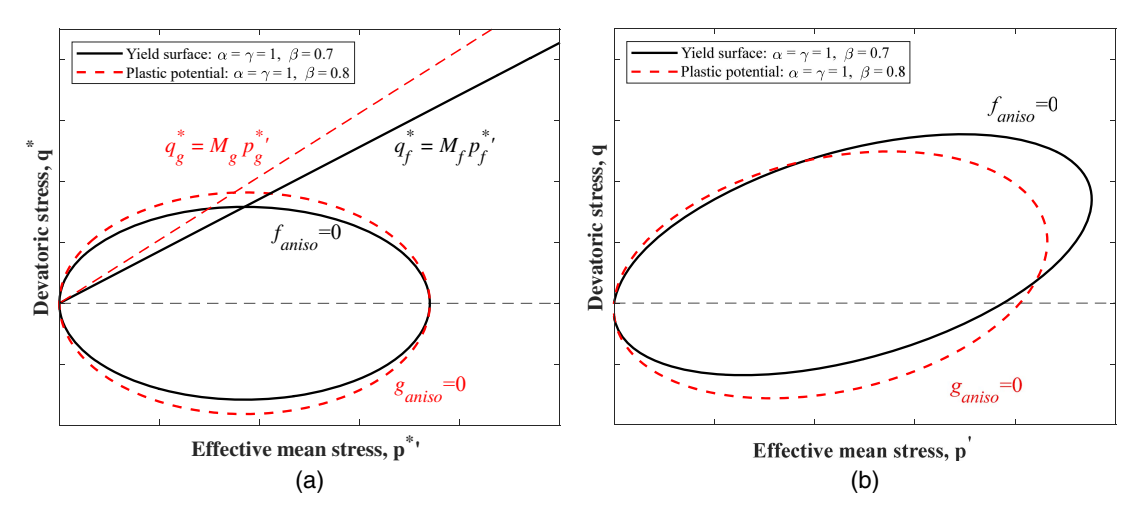


Fig. 3. Overview of anisotropic yield surface and plastic potential of MCC model in: (a) $p'^* - q^*$ spaces; and (b) p' - q spaces; where $\alpha = \gamma = 1$, and $\beta = 0.7$ for yield surface, and $\alpha = \gamma = 1$, and $\beta = 0.8$ for plastic potential.

Table 1. Dependent parameters used in the non-isothermal multiphase flow equations

Parameter	Equation
Variations of intrinsic permeability with porosity (Chapuis and Aubertin 2003)	$ \kappa_{\text{int},i} = \kappa_{\text{int},i0} \left(\frac{1-n_0}{1-n}\right)^2 \left(\frac{n}{n_0}\right)^3, i = \ \text{ or } \perp $
Relative permeability of water (Mualem 1978)	$\kappa_{rw} = S_{eff}^{\lambda_r}$
Saturated vapor density (Bittelli et al. 2015)	$\rho_{v,sat} = 0.001T^{-1} \exp(31.37 - 6014.79T^{-1} - 0.00792T)$
Binary vapor diffusion coefficient (Bittelli et al. 2015)	$D_v^0 = 2.92 \times 10^{-5} (T/273.15)^2$
Tortuosity (Lai et al. 1976)	$\tau = [n(1 - S_w)]^{2/3}$
Latent heat of vaporization (Monteith and Unsworth 2013)	$L_v = 2.501 \times 10^6 - 2369.2(T + 273.15)$
Thermal conductivity of the medium (Bittelli et al. 2015)	$\lambda_{eff} = nS_w \lambda_w + n(1 - S_w)\lambda_g + k_s(1 - n)\lambda_s$
Volumetric heat capacity of the medium (Bittelli et al. 2015)	$(\rho C)_{eff} = nS_w(\rho C)_w + n(1 - S_w)(\rho C)_g + (1 - n)(\rho C)_s$

In the case of isotropic materials where m = 1, Eq. (31) becomes $\kappa_{\text{int}} = \kappa_{\text{int}} 1$.

For unsaturated soils, a constitutive relationship (SWR model) must be defined between the matric suction and water content. Several SWR models were proposed for different soils that account for different aspects of thermo-hydro-mechanical behavior. Van Genuchten (1980) proposed one of the most frequently used SWR models (the VG model) to predict the soil-water retention curve in different soils and rocks. The VG model has been modified in different studies to account for non-isothermal conditions (Grant and Salehzadeh 1996; Vahedifard et al. 2018), oven-dry saturation regime (Zhang 2011), and deformable soils (Gallipoli et al. 2003; Tarantino 2009). In this study, the VG model is incorporated to analyze a natural clay (i.e., Boom clay) with the following assumptions: First, the SWR characteristic curve ignores the soil's deformability. This hypothesis is supported by the experimental observation presented by Della Vecchia et al. (2010), who conducted a Mercury Intrusion Porosimetry (MIP) test, and found that the initial fabric of natural Boom clay shows a clear unimodal pore size distribution. They also found that although drying an undisturbed sample of Boom clay changes the pore size of the sample, drying did not alter the topology of the void space. However, this hypothesis is not valid for soils with two dominant pore sizes or double porosity features. The effect of double porosity in the different hydromechanical paths has been investigated in other studies (Sánchez et al. 2005). Second, we assumed that non-isothermal effects have a negligible effect on the SWR curve, because the range of temperature changes due to the latent heat of vaporization is small during convective drying. Third, the effect of hysteresis during wetting/drying is ignored, because only the drying process is considered in this study. Finally, the matric suction is assumed to be approximately equal to capillary pressure ($p_c = p_a - p_w$). Therefore, the VG model is expressed in Eq. (32) as

$$S_{eff} = \left[1 + \left(\frac{p_c}{\alpha_{VG}}\right)^{n_{VG}}\right]^{-m_{VG}} \tag{32}$$

where α_{VG} (ML⁻¹T⁻²) is related to the air-entry value of the soil; and n_{VG} and m_{VG} are the SWR constants.

In this section, a coupled non-isothermal multiphase flow with related mechanical and hydraulic constitutive models is presented in detail. Table 1 contains all the dependent parameters used in this section.

Description of Convective Drying and the Experimental Investigation

Convective Drying

Equilibrium methods (e.g., the vapor equilibrium technique) are often used to model the drying experiments of geomaterials (Blatz et al. 2008; Tang and Cui 2005). Although these experimental methods provide important insights about the final stage of the evaporation process (steady-state of evaporation), they neglect the

thermo-hydro-mechanical evolution of drying kinetics, such as thermal exchange at the soil-atmosphere interface, rate of evaporation, and possibly crack initiation. Therefore, convective drying techniques are more appropriate to model the natural evaporation from bare soils (Musielak and Mierzwa 2009). As stated before, evaporation from saturated soils involves two distinct stages. In the first stage, a high evaporation rate can be observed due to the water availability of the soil medium, and the second stage is marked by a drastic reduction of the evaporation rate and by receding of the drying front from the soil-atmosphere surface deeper into the soil. In the second stage of evaporation, the temperature increases close to the evaporation boundary. Tamizdoust and Ghasemi-Fare (2020c) concluded that when the soil dries out thermal conductivity is decreased if vapor cannot properly transfer heat in this region, and consequently, the soil's temperature is increased. Recently, attempts have been made to couple free flow and fluid flow in a porous medium, which have produced relatively accurate results (Vanderborght et al. 2017). However, this method is computationally demanding. An alternative and simpler approach, which has long been used in different studies, is called the boundary layer model (Brutsaert 2005). In this approach, a boundary layer with a finite width is assumed, in which mass and heat transfer take place convectively.

The boundary layer model appears as the soil-atmosphere boundary condition for Eqs. (9) and (10) in the numerical analysis. We can introduce the mass transfer boundary condition for Eq. (9) as

$$E = m_v[(\rho_{v,eq})_{surf} - (\rho_{v,eq})_a]$$
(33)

where E (ML⁻²T⁻¹) is the rate of vapor mass transfer from the soil-atmosphere boundary; m_v (LT⁻¹) is the mass transfer coefficient; and $(\rho_{v,eq})_{surf}$ (ML⁻³) is the equilibrium vapor density of the soil medium at the surface boundary; and $(\rho_{v,eq})_a = (\rho_{v,sat})_a \times (RH)_a$, where subscript a stands for atmosphere, and $(RH)_a$, $(\rho_{v,eq})_a$, and $(\rho_{v,sat})_a$ are the relative humidity, equilibrium, and saturated vapor densities of the atmosphere. The mass transfer coefficient, m_v , can be calculated experimentally, as well as by numerical and analytical approaches (Choudhury et al. 1986; Gerard et al. 2010; Sviercoski et al. 2018).

The thermal energy exchange across a natural soil-atmosphere boundary can be influenced by solar radiation, latent heat of evaporation, and sensible heat flux (Bittelli et al. 2015), and is illustrated in Fig. 1. In the controlled convective drying experiment, one can disregard solar radiation; therefore, the energy balance equation (EBE) can be defined as

$$G = -m_h(T_{\text{surf}} - T_a) - L_v E \tag{34}$$

where G (MT⁻³) is the surface heat flux from the top boundary; m_h (MT⁻³ Θ^{-1}) is the convective heat transfer coefficient, which can be determined experimentally; T_a is the temperature of the atmosphere; and T_{surf} is the soil's surface temperature. The first term on the right hand side of Eq. (34) is the sensible heat flux, the second term is the latent heat of evaporation, and the negative signs denote the outgoing fluxes. Eq. (34) serves as a boundary condition in Eq. (10).

Microconvective Drying Experiment

This study aims to present a thermo-hydro-mechanical model that can be utilized to analyze the convective drying of clayey soils. The numerical model was validated with an experiment on drying-induced shrinkage of Boom clay, a natural clayey rock (Hubert et al. 2018; Prime et al. 2015), and the numerical and experimental

results were compared at different stages of the drying process. A brief description of the experiment is now outlined.

- Sample preparation: A clay sample was drilled out of a borehole that was located at an underground research facility (220 m below the ground) in Mol, Belgium (Prime et al. 2015). The coring was conducted in the direction parallel to the bedding planes; therefore, the geometrical overview of the sample is visualized in Fig. 6. The clay sample was saturated with water with a chemical composition similar to the in-situ condition in a triaxial device under an effective stress state identical to the in situ stress state (identical confinement). A water pressure gradient of 1 MPa applied in parallel to the bedding planes led to a full saturation after 40 days (Prime et al. 2015). After saturation, the core sample was cut into several smaller cylindrical samples with different dimensions. All these smaller samples were dipped in paraffin. The paraffin was then removed from the top of the cylindrical samples for the drying experiment, so that the evaporation occurred only from the top surface.
- Microconvective drying device: The samples were placed in a microconvective drying device where a constant airflow with controlled temperature and relative humidity was imposed on the top surface of the samples. The microconvective drying was designed in the Laboratory of Chemical Engineering at the Université de Liège, to study the drying of different materials, such as wastewater sludges, mortar cement, etc. (Prime et al. 2015). The experiment was done in a way to mimic the ventilation of an underground gallery, where the host rock (i.e., Boom clay) dries only from one side and the air flow is parallel to the drying surface.
- Data acquisition: The mass of the samples was measured every 30 s during the drying process. Measurements of the volume, cracking, cross-sectional surface area, and radii of each sample were carried out by analysis of the tomographic reconstructions. An X-ray radiation technique was used for this non-destructive data acquisition. In order to scan the samples during the experiment, drying had to be halted, and the samples had to be removed from the apparatus and scanned by a tomography device. Weighing of the samples before and after the scanning showed less than 1% of mass loss, which was acceptable. All samples were also scanned in saturated and dry states. A precise procedure was used to find the cross-sectional area of the samples, by distinguishing the pixels of the cross-sectional image of the sample representing the clay, the voids that appeared by cracks, and the outer boundary of the sample. To measure the evolution of the samples' shrinkage, parallel and perpendicular radii of the cylindrical samples were measured, by finding enclosing circles on every axial cross-section and their centers, which led to finding the cylindrical axis. Then, the cylindrical axis was used to transform the Cartesian coordinates (x, y, z) system to cylindrical ones (r, φ, z) on the sample interface points, where r is the distance from the cylindrical axis, z is the height along the axis, and φ is the azimuth angle around the axis. $\varphi = 0$ was chosen to be parallel to the bedding plane. The set of interface points on the basis of height and angle were used to determine the average radius in two perpendicular directions.

More details of the experimental procedure and the data acquisition are provided in Prime et al. (2015) and Hubert et al. (2018).

Thermo-Hydro-Mechanical Properties of Unsaturated Boom Clay

Boom clay is an anisotropic stiff clay with a moderate plastic limit, which due to its thermo-mechanical properties was found to be a suitable natural clay barrier for nuclear waste repositories in

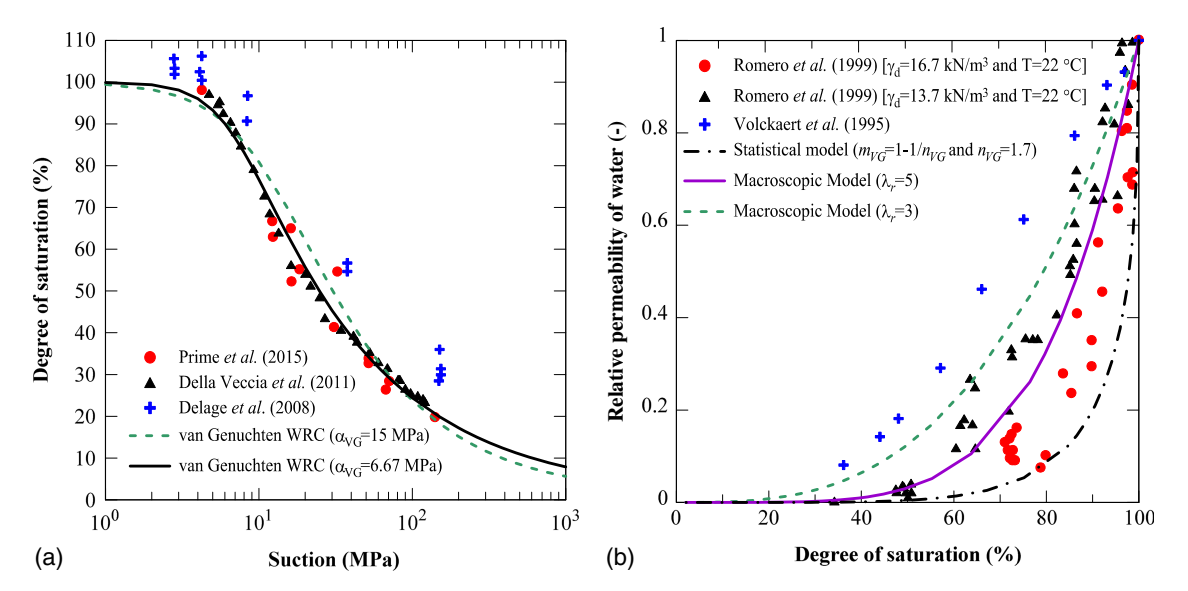


Fig. 4. Experimental data and analytical relations for: (a) soil-water retention curve; and (b) relative permeability of water for unsaturated Boom clay.

Belgium (Bernier et al. 2007). In the past three decades many experimental programs have been conducted to understand the thermal, hydraulic, and mechanical behavior of natural and compacted Boom clay in both saturated and unsaturated conditions (Baldi et al. 1991; Delage et al. 2000; Horseman et al. 1987; Le et al. 2008; Romero et al. 1999; Volckaert et al. 1995). Figs. 4(a and b), respectively, illustrate some of the experimental data for the SWR characteristics and relative permeability of water for Boom clay. The experimental data in Figs. 4(a and b) were used to calibrate the VG parameters for the current study. The comparison between the macroscopic and the statistical (van Genuchten-Mualem model) approaches for calculating the relative permeability of water for Boom clay is presented in Fig. 4(b). In this study, a better agreement is observed between the relative permeability of water obtained by the macroscopic approach and the experimental measurement. The fitting parameter (λr) should be calibrated based on the experimental observations. Mualem (1978) suggested a lower bound of 2.5 for coarse-grained and an upper bound of 24.5 for very fine-textured soils. However, recently other researchers utilized a lower value $(\lambda r = 3)$ for other fine-grained soils such as FEBEX bentonite, based on the experimental observations (Sánchez et al. 2012, 2016). In this study, λr is calibrated by comparing numerical and experimental results on Boom clay. As is shown in Fig. 4(b), $\lambda r = 5$ shows a better agreement for Boom clay.

Table 2 provides the thermo-hydraulic properties of the Boom clay used in the presented numerical analysis, all of which are in accordance with the values reported in the literature (Della Vecchia et al. 2010; François et al. 2009; Tamizdoust and Ghasemi-Fare 2020b). The mass and heat transfer coefficients are taken from Prime et al. (2015).

Parameters related to yielding and stress-dilatancy can be obtained from the triaxial test results performed by Sultan et al. (2010) on natural Boom clay. Sultan et al. (2010) stated that according to their experiment the direction of the plastic strain increments did not obey the normality rule of plastic flow; thus, non-associativity is assumed for this study. Fig. 5(a) compares the experimental observation of the stress-dilatancy relationship for natural and isotropically loaded specimens up to 9 MPa with the results obtained from the analytical expression presented in Eq. (27). Experimental stress-dilatancy data for natural and isotropically loaded Boom clay are used to calibrate the stress ratio

Table 2. Thermohydraulic properties of unsaturated natural Boom clay

Parameter	Value	Unit
$\overline{n_0}$	0.39	m^3/m^3
$\kappa_{0int,\parallel}$	5×10^{-19}	m^2
$\kappa_{0{ m int},\perp}$	2.5×10^{-19}	m^2
μ_w	0.001	Pa · s
c_w	4.5×10^{-10}	1/Pa
α_{VG}	6.67	MPa
n_{VG}	2.8	_
m_{VG}	0.19	_
S_r	0.01	_
λ_r	5	_
ρ_{w0}	998.2	kg/m ³
ρ_{s}	2,670	kg/m^3
C_w	4,185	J/kg/°C
C_w C_g C_s	2,062	J/kg/°C
$C_{\mathfrak{s}}$	750	J/kg/°C
λ_w	0.59	W/m/°C
λ_g	0.026	W/m/°C
λ_s^{σ}	1.7	W/m/°C
α_w	3×10^{-4}	1/°C
α_d	1.3×10^{-5}	1/°C
m_v	0.048	m/s
m_h	53	W/m ² /°C

at the critical state (M_g), and the model parameters (i.e., α , β , and γ), which are incorporated in the projection tensor for plastic potential function. Fig. 5(b) illustrates that the rotated/distorted plastic potential function [Eq. (25)] and yield surface [Eq. (28)] obtained from analytical expressions match well with the experimental observations presented in Figs. 5(a and b). The values of α , β , and γ , which are utilized to construct the projection tensor for a yield function, are obtained based on the experimental yielding stresses [circles in Fig. 5(b)]. Moreover, the initial preconsolidation pressure and the stress ratio at the critical state are in accordance with the values reported by Sultan et al. (2010).

The thermo-mechanical properties of unsaturated natural Boom clay are reported in Table 3. The parameters for the anisotropic thermoporoelastoplastic constitutive model are taken from previous research work (Della Vecchia et al. 2010; François et al. 2014, 2009; Hubert et al. 2018; Le Pense et al. 2016).

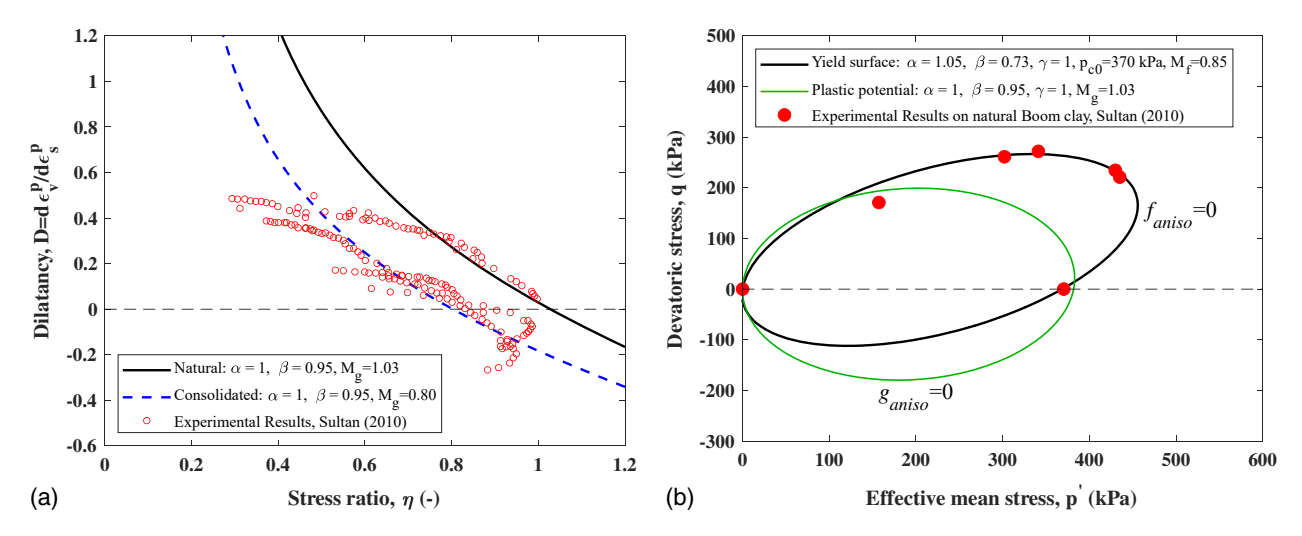


Fig. 5. Experimental data and analytical relations for: (a) stress-dilatancy; and (b) plastic potential and yield surface for natural Boom clay.

Table 3. Properties of the anisotropic thermoporoelastoplastic model

Parameter	Value	Unit
$\overline{E_{\parallel,ref}}$	400	MPa
$E_{\perp,ref}$	200	MPa
$ u_{ }$	0.125	_
n_e	0.8	_
p_{ref}	2.25	MPa
p_{c0}	0.37	MPa
	0.03	_
$eta_p \ b_1$	0.1	_ _ _
b_2	2	_
γ_T	0.55	_
M_g	1.03	_
M_f^g	0.85	_

Numerical Simulation

The presented coupled equations governing the multiphase flow in deformable soils were simultaneously solved to analyze the convective drying experiment on Boom clay. The Structural Mechanics module in COMSOL Multiphysics software v5.3a (COMSOL 2018) was modified to implement the transversely anisotropic constitutive model described in previous sections. Eq. (9) was implemented in the General PDE module to account for vapor flux as well as thermal and mechanical coupling terms. The Heat Transfer in the Porous Media module was used to solve Eq. (10) for the multiphase flow. A 3D cylindrical domain was required due to the anisotropic deformation in parallel and perpendicular directions to the bedding planes. The geometrical model was discretized using hexahedral elements in COMSOL. Fig. 5 presents the finite element mesh, with a total of 3,135 elements after mesh sensitivity analysis. The Boom clay was initially saturated and stress-free. Also, the initial temperature of the sample is considered to be 17°C. According to the experimental procedure, no fluid mass exchange nor heat transfer occurred from the bottom or circumference of the cylinder; therefore, no mass flow and no heat flux are imposed at these boundaries. Vertical displacements were prevented at the bottom boundary, and all the external boundaries were subjected to atmospheric pressure. The top boundary was exposed to the environmental evaporative force. The speed of the airflow was 0.8 m/s and its temperature and relative humidity were kept constant at 25°C and 3.5%, respectively. The extremely low relative humidity indicates that a high suction value (about 480 MPa) was applied at the top surface. The height and radius of the numerical cylindrical model were calculated referring to the experimental observations for the initial surface, mass, and radii of the sample. This procedure was necessary to ensure a consistent initial geometrical state. The geometry and boundary conditions are summarized in Fig. 6. The model was solved using the PARDISO (parallel sparse direct solver) of COMSOL Multiphysics, which takes advantage of all processor cores on a single machine and can store the solution out-of-core, which means that it can offload some of the solving procedure onto the hard disk (COMSOL 2018). The relative tolerance for the nonlinear analysis was set to 0.001.

Results and Discussion

In the following, the numerical results of convective drying of natural Boom clay are compared and validated with the experimental observations from Prime et al. (2015) and Hubert et al. (2018). Figs. 7 and 8 compare the drying kinetics of Boom clay in terms of mass loss and drying rate obtained from numerical and experimental models. Mass loss can be estimated from the volume-average density among all the phases of the system (density of the soil skeleton) divided by the updated volume of the sample at each time step. The drying rate can be defined as the rate of mass loss divided by the updated top surface, also called the evaporative boundary:

$$Q_f = -\frac{1}{S(t)} \frac{dm_f}{dt} \tag{35}$$

where Q_f (ML⁻²T⁻¹) is the drying rate; dm_f/dt (MT⁻¹) is the rate of fluid mass change; and S(t) (L²) is the top surface area at each time step. The subscript f refers to a fluid. The comparison of the numerical results with the experimental observations presented in Figs. 7 and 8 confirms the accuracy of the developed THM model. Root Mean Square Error (RMSE) and non-dimensional forms of RMSE known as Normalized Root Mean Square Error (NRMSE) have frequently been used in the literature to evaluate model performance through a quantitative comparison between numerical and experimental data. For the results presented in Fig. 7(a), RSME = 0.0146 and NRMSE = 0.048. Moreover, for the results presented in Fig. 8(a), RSME = 0.000023 and NRMSE = 0.056.

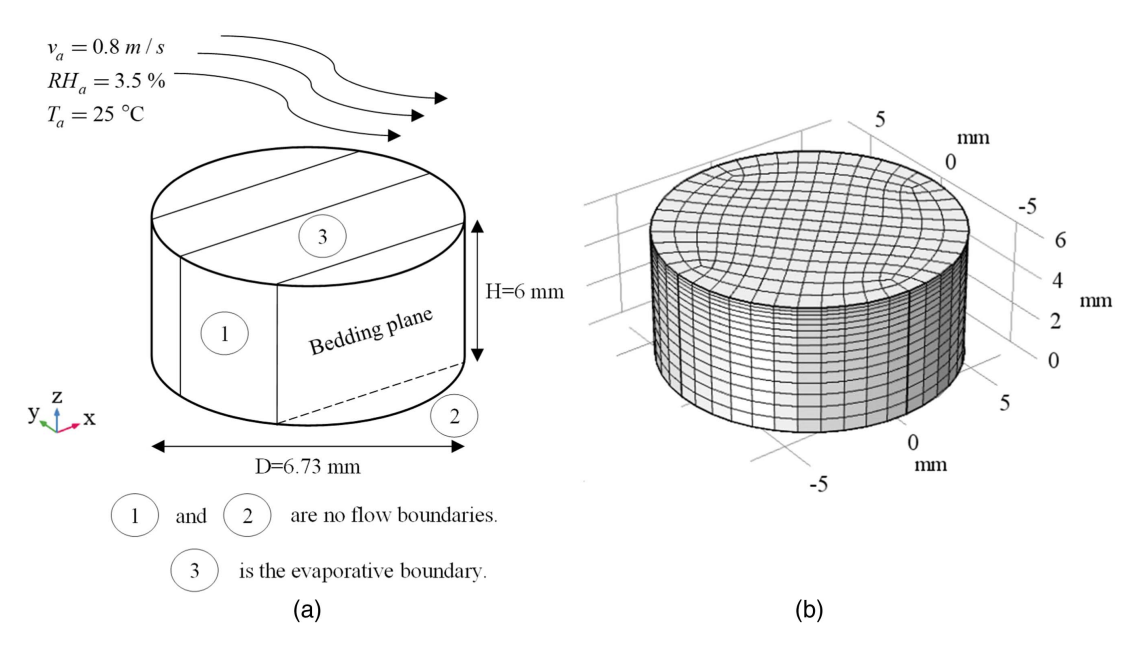


Fig. 6. Schematic illustration of the clay sample: (a) geometry and boundary conditions in the experimental model; and (b) discretization of the numerical model.

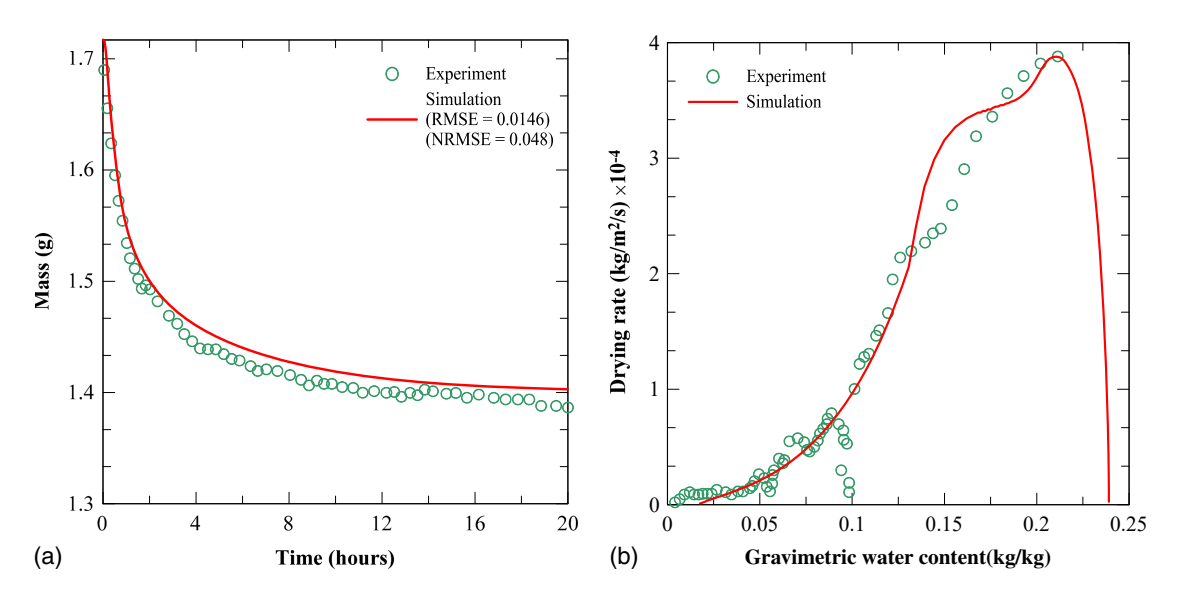


Fig. 7. Comparison of simulated and experimental results for drying kinetics: (a) mass loss; and (b) drying rate (Krischer curve).

In addition, as the hydraulic properties of the soil, such as the intrinsic and relative permeability of water, have direct effects on the evaporation process, it can be concluded that the hydraulic properties and the SWR constitutive model used in this study adequately simulated the drying experiment.

Figs. 8(a and b) demonstrate the experimental and simulated results of the drying rate and liquid and vapor flux participation in the total fluid flux during the 20 h of the experiment. The experimental data shows an abrupt decrease in the drying rate almost at the beginning of the test while no distinct constant drying rate (first stage of drying) could be seen. The loss of liquid connection between the drying front and evaporative surface marks the end of the constant drying rate period. Fig. 8(a) shows that the simulated curve fits well with the experimental results. The numerical model can also illustrate the start of the drying process, where the drying

rate increases. From Fig. 8(b), it is evident that liquid flux governed by Darcy's flow increases to its maximum value to deliver the water to the evaporation surface and meet the evaporative demand of the atmospheric condition. After that, the water availability at the surface (i.e., top boundary) is reduced and fluid flow is governed by Fick's law of vapor diffusion (which in this test occurred after almost two hours of the drying process). In this case, the evaporation is controlled by the hydraulic properties of the medium. Vapor diffusion occurs at a slower pace until the capillary water is evaporated. The depth of the drying front from the evaporative surface (i.e., critical length of the liquid connection) can be calculated based on the theoretical formulation proposed by Lehmann et al. (2008). From the drying rate results in Fig. 8(a), it can be seen that, for the sample size considered in this study, the liquid connection between the drying front and the evaporative surface is disrupted

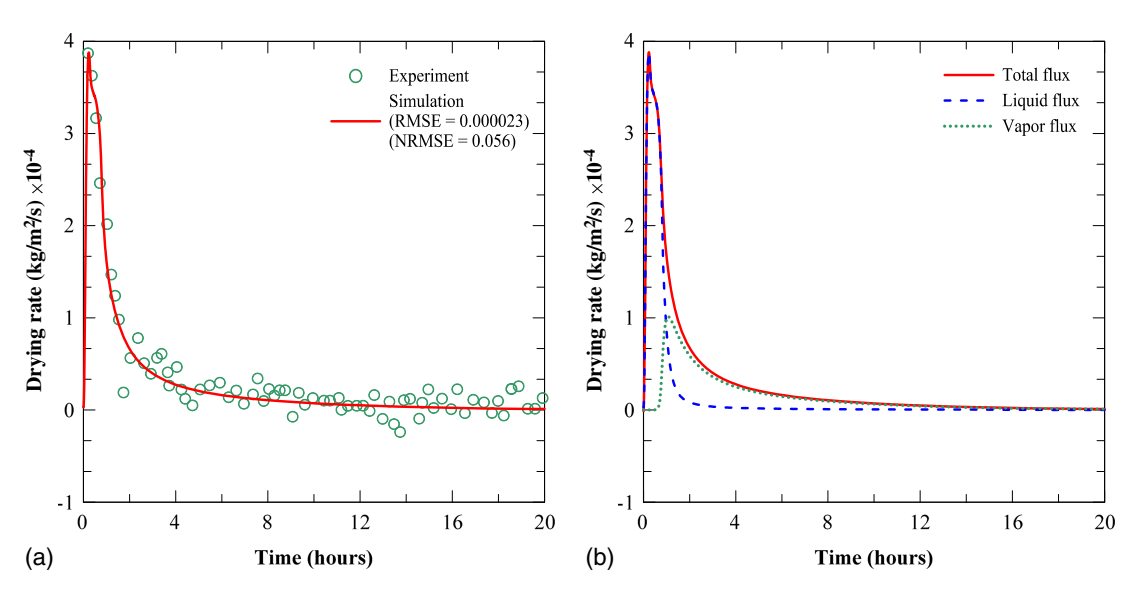


Fig. 8. Comparison of simulated and experimental results for drying kinetics: (a) drying rate versus time; and (b) contribution of liquid and vapor flux to drying rate.

immediately after the beginning of the experiment, which means that the critical length of the liquid connection is less than the sample size considered here, as previously indicated by Hubert et al. (2018). For the same reason and under the same environmental evaporative demand, a constant drying rate period in a larger sample size is even less likely to be observable, because the critical length of the liquid connection is an intrinsic property of the porous medium and does not change with the domain's dimensions. However, it should be noted that the first stage of evaporation under a low atmospheric evaporative demand (<5 mm/day) can be extended for days despite the gradual desaturation of the soil's surface and the receding of the drying front (Or et al. 2013). On the other hand, for a high evaporative demand (e.g., >5 mm/day), the evaporation rate is expected to continuously decrease during the first stage of evaporation for both coarse and fine soils even when the soil's surface is saturated (Shahraeeni et al. 2012). These findings emphasize the complex soil-atmosphere interaction and its impact on the evaporation rate. Thus, for large-scale and real-world applications, the dynamics of atmospheric evaporative demand and the intrinsic hydraulic properties of the soil (e.g., pore size, air entry value, etc.) should be carefully taken into account.

Fig. 9 shows the average temperature of the specimen with respect to time. Only the numerical result is presented, because the sample temperature was not measured during the experiment (Hubert et al. 2018). According to Fig. 9, the temperature drops to a minimum value of about 8°C (temperature of the wet bulb) from its initial value of 17°C. The drop in the temperature of the sample is because of the latent heat of vaporization. The evaporation that is triggered by the volume of dry air leads to a decrease in temperature, while the vapor pressure increases due to evaporation. Thus, the temperature almost immediately increases to become equilibrated with the temperature of the dry airflow (25°C). The absence of a constant temperature at the wet bulb is in accordance with the absence of the first stage of evaporation or constant drying rate period.

The experimental and simulated results of the drying-induced shrinkage are presented in Fig. 10. Fig. 10(a) shows the shrinkage of the top surface and Fig. 10(b) shows the normalized volumetric shrinkage during the drying process. As can be seen in Figs. 10(a and b), although slightly higher volumetric shrinkage

is predicted in comparison to the experiment, the numerical model can capture the experimental data points with reasonable accuracy. Fig. 10(c) describes the volumetric shrinkage of the sample and the evaporation volume against the average gravimetrical water content. The volumetric shrinkage is the difference between the current (updated at each time step) and initial volumes, and evaporation volume is calculated as mass loss divided by water density. Compared to the experimental measurement, the simulated results are acceptable. Although the volumetric shrinkage is slightly overestimated compared to the experimental observation, it follows the same trend. The evaporation and shrinkage volumes overlap until the gravimetric water content is lowered to 0.2, as experimentally reported by Prime et al. (2015). During the early stage of drying the contraction of the pores is equal to the volume of water expelled from the multiphase system, which indicates evaporation occurs without desaturation (called normal shrinkage). Beyond this point (i.e., where gravimetric water content equals 0.2), the evaporation

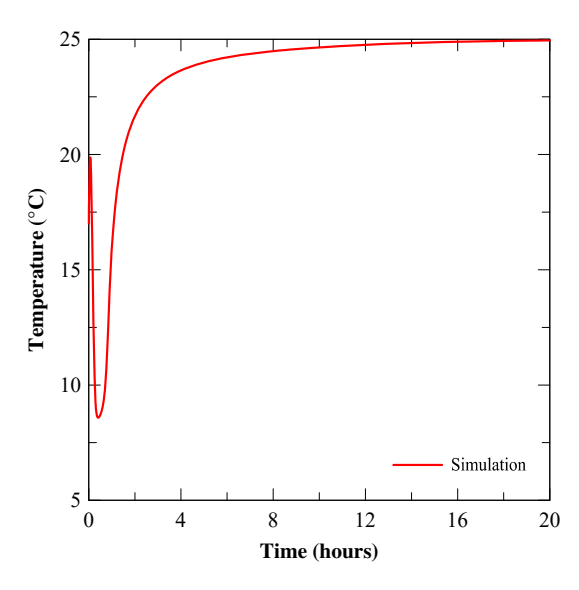


Fig. 9. Average temperature variation of the sample during drying simulation.

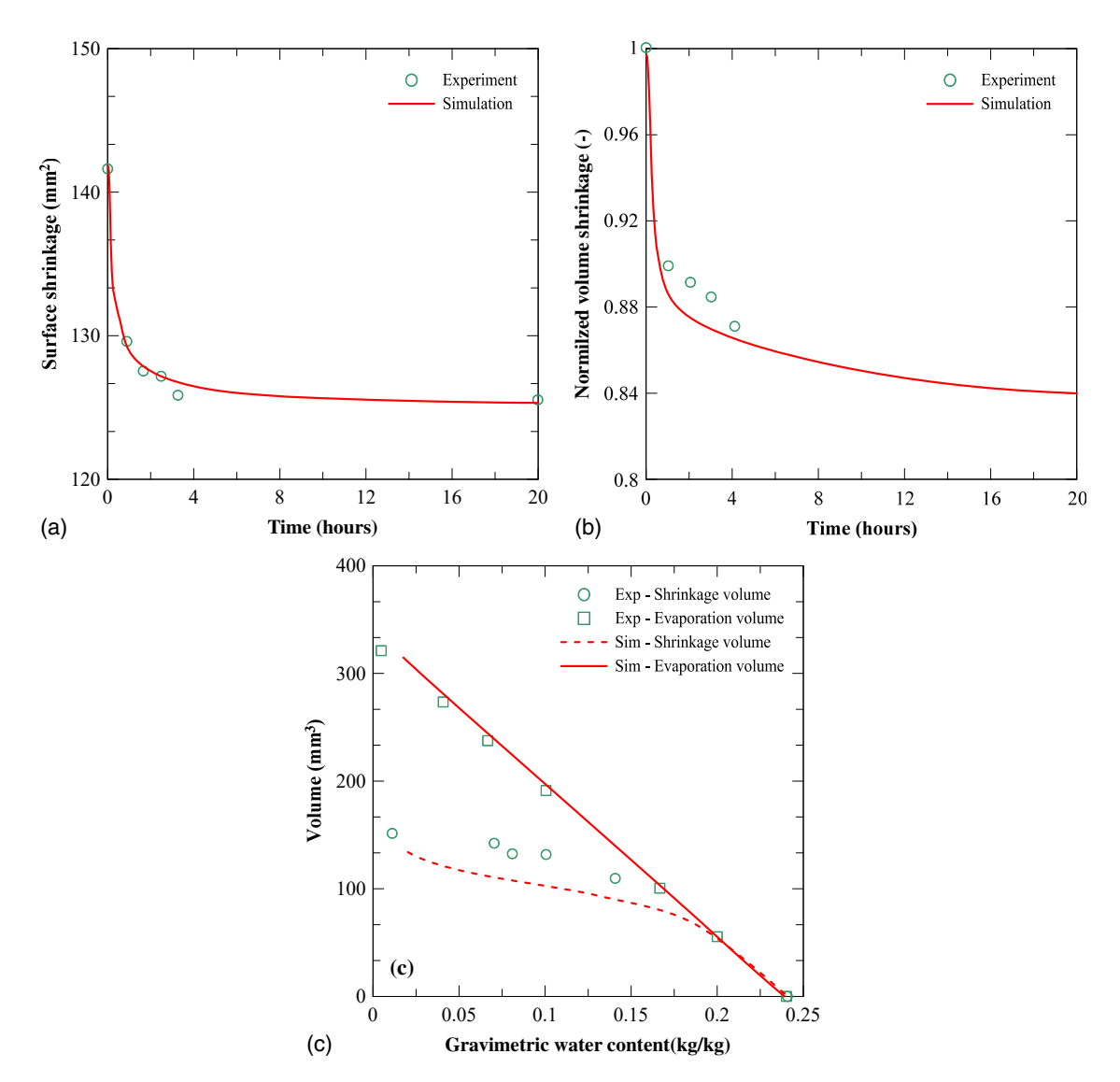


Fig. 10. Comparison of simulated and experimental results for drying-induced shrinkage: (a) surface; (b) normalized volumetric shrinkage; and (c) volumetric evaporation and shrinkage curves.

volume is normally linear while the slope of the pore skeleton shrinkage is reduced due to drying-induced hardening of the soil. The mathematical model presented in this study shows a decent capability to reproduce the observations of the drying-induced shrinkage in a fully-controlled experiment.

The following presents the variations in the degree of saturation, porosity, top surface anisotropic shrinkage, and volumetric deformation obtained from the THM model during the different stages of the drying process. Fig. 11 demonstrates the percentage of saturation at different times. The unbalanced and nonhomogeneous distribution of the degree of saturation (water content) is observable after one hour of the drying process, with almost a 60% difference from the top to the bottom of the sample (from 20.1% to 81.4%). The difference becomes less pronounced at later times when most of the water has evaporated from the sample and uniform water content distribution is almost reached (from 12.5% to 14.5%). The degree of saturation is calculated based on the adopted SWR characteristics and subsequent fitting parameters, although the same behavior is expected to be observed in different SWR models.

The drying-induced shrinkage of the Boom clay is analyzed by referring to porosity variation at different times of the experiment.

The changes in the porosity of the sample during the 20 h of the experiment are presented in Fig. 12. As can be seen, most of the deformation occurs in the first hour of the experiment, which was also found by Prime et al. (2015). Comparing the result obtained after 20 h with the initial state of the sample reveals an almost 30% reduction in porosity. The anisotropic shrinkage of the sample is also evident in Fig. 12, which compares the geometrical size of the model with respect to the initial dimension shown by a frame in Figs. 12(a-d). Nonuniform and nonsymmetric shrinkage occurs due to transient and fast evaporation from the top surface and utilizing the transversely isotropic constitutive model, respectively. The plan view of the top surface during the 20 h of the drying process can better present the anisotropic shrinkage (Fig. 13). Fig. 13 illustrates the shrinkage of the top surface (shown in dark line) and the initial surface (shown in dashed gray line) at different time steps. Please note that, because after one hour of shrinkage the difference in the deformation of the top and the bottom boundaries is small, only the shrinkage of the top surface is presented. Fig. 13 clearly shows that the circular shape of the sample is deformed into an elliptical surface.

According to Eq. (5), the porosity variations are directly related to the total volumetric strain. Fig. 14 presents the contribution of

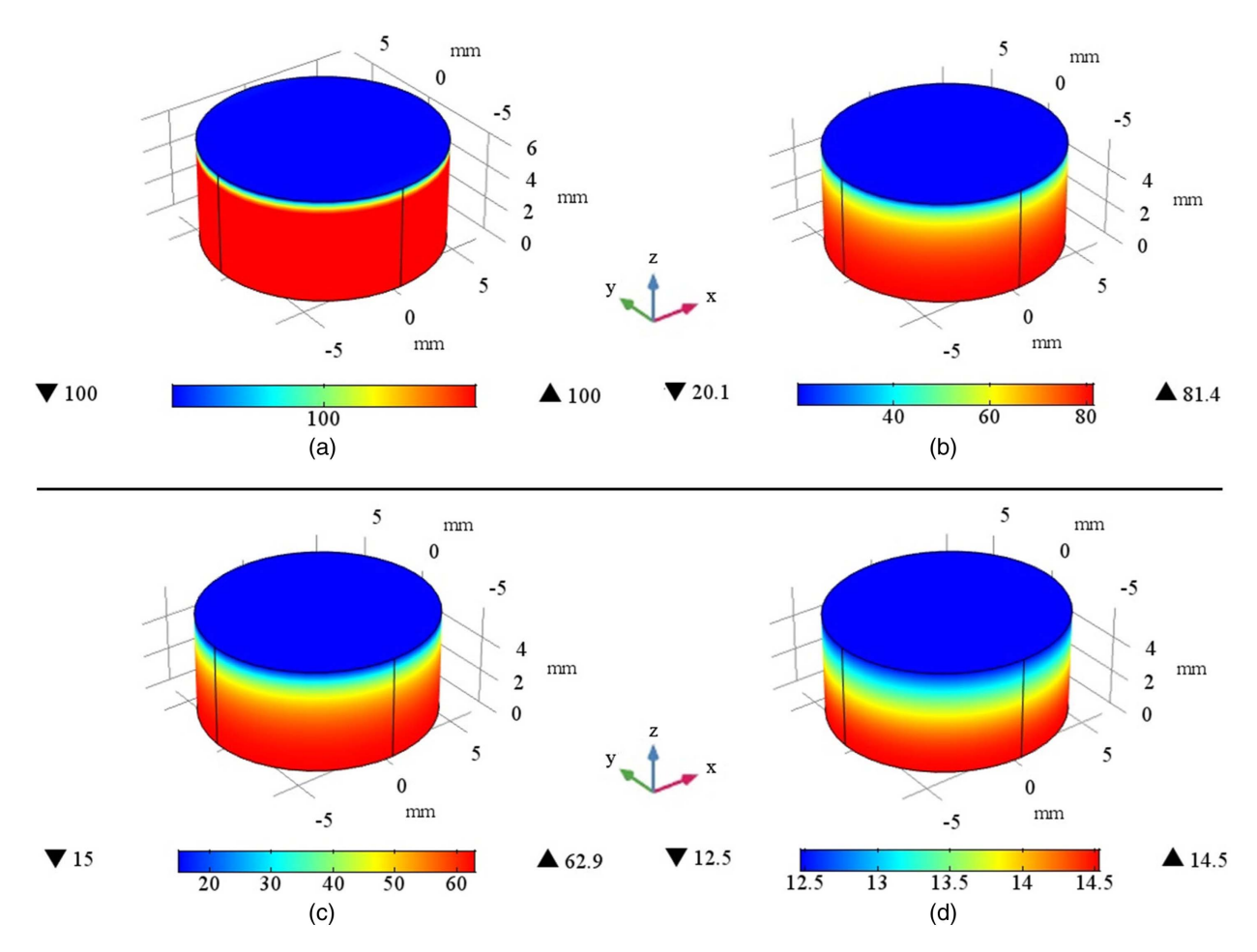


Fig. 11. Variations in saturation at different times: (a) initial state; (b) after one hour; (c) after two hours; and (d) after 20 h.

the volumetric elastic (about 18%) and plastic (about 82%) strains to the total volumetric deformation after 20 h. With respect to the small range of temperature change, the volumetric thermal strain after 20 h is only 0.03%. The numerical results demonstrate that the contribution of the anisotropic plastic strain is significantly higher than that of the anisotropic elastic strain. According to Eq. (19), Young's moduli parallel and perpendicular to the bedding planes non-linearly and rapidly increase at higher isotropic pressures. This feature results in relatively low volumetric elastic deformation compared to the plastic deformation. For unsaturated soils, Young's modulus is usually determined experimentally at different moisture contents (Yang et al. 2012). However, due to the lack of experimental information on direct variations of Young's modulus at different moisture contents for Boom clay, we employed Eq. (19), which has been incorporated for unsaturated soils in different studies (François and Laloui 2008). In addition, the current model considers the effects of both the strain-hardening due to plastic deformation, and suction-hardening during the desaturation on the volumetric plastic strain [Eq. (29)]. Material parameters are all borrowed from previous studies on Boom clay, to yield more realistic results.

In addition, a sensitivity study was performed to explore the effect of Young's and plastic compressibility moduli on the drying shrinkage of a transversely isotropic clay. Figs. 15(a and b) present the impact of constant and variable Young's moduli and plastic compressibility modulus on the surface shrinkage of Boom clay and compare the numerical results with the experimental

measurements. The constant Young's moduli are equal to the reference values presented in Table 3. The variable Young's moduli, which rapidly increase with increasing mean effective stress, are calculated according to Eq. (19). In Fig. 15(a), a comparison is made between elastoplastic and elastic models. In the elastic model, it is evident that although utilizing the constant Young's moduli reasonably predicts the early stage deformation, it leads to the underestimation of clay stiffness at high suction values (evidenced by larger final surface shrinkage), and cannot be used as an appropriate approximation of the soil's shrinkage during convective drying. On the other hand, considering only the elastic model with variable Young's moduli substantially underestimates surface shrinkage. In Fig. 15(b), different values of plastic compressibility modulus in terms of the difference in the slope of the dryinginduced compression line and swelling line $(\lambda - \kappa)$ are shown. The increase in the difference of λ and κ is a direct consequence of suction-induced hardening that leads to a stiffer material. By incorporating $(\lambda - \kappa = 0.01)$ and $(\lambda - \kappa = 0.1)$ in model simulations, the results in Fig. 15 (b) show either too stiff or too soft material. When the difference between the slopes of the drying-induced compression line and the swelling line is doubled (i.e., $\lambda - \kappa = 0.1$), approximately 10% more reduction in the final surface shrinkage is observed. Further, a comparison of the results in Figs. 15(a and b) shows that the deformation of natural Boom clay under the described condition is very sensitive to both the plastic compressibility and the elastic moduli. Thus, careful calibration of the parameters from experimental data is needed (and done in

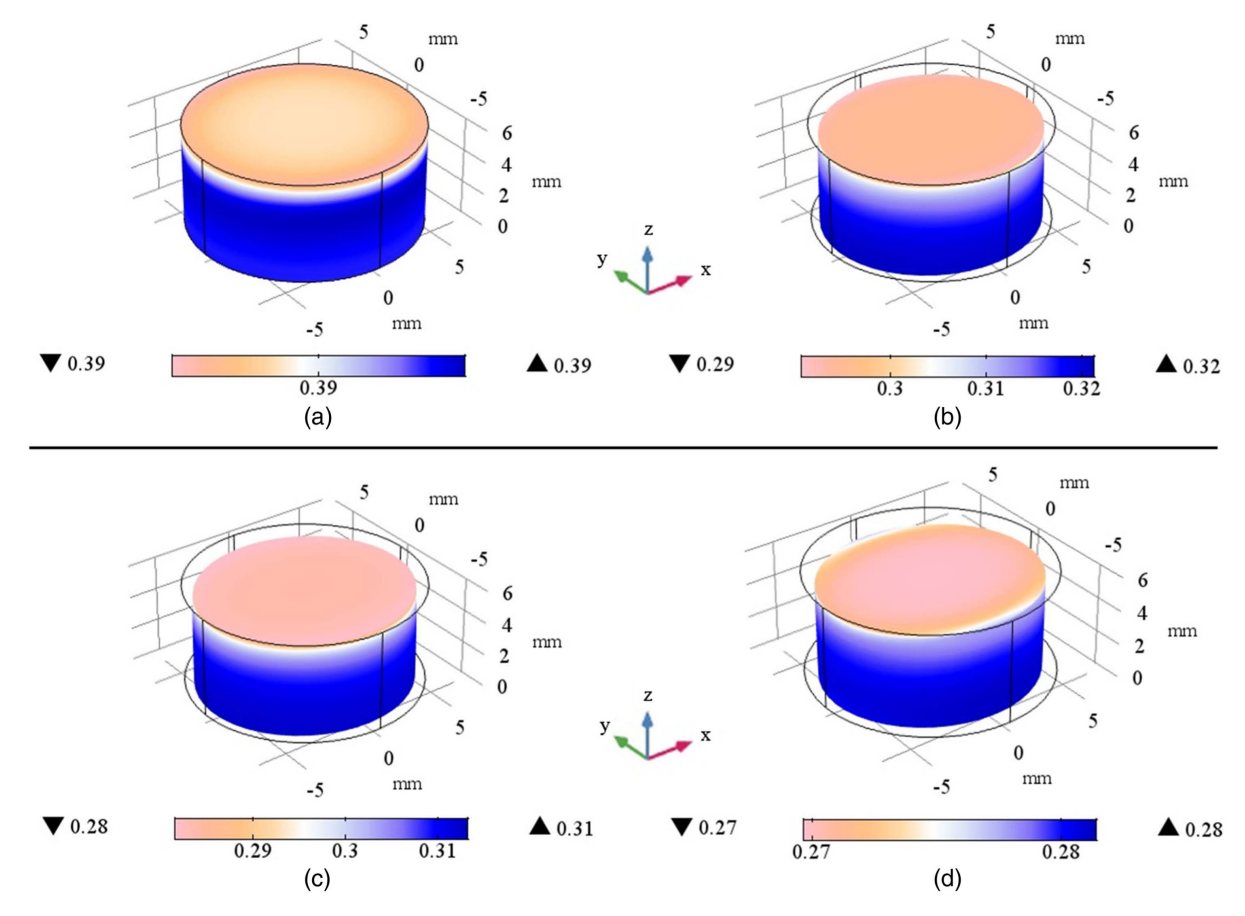


Fig. 12. Variations in porosity at different times: (a) initial state; (b) after one hour; (c) after two hours; and (d) after 20 h.

this study), for meaningful evaluation of Boom clay's deformation under convective drying.

The evolution of the parallel and perpendicular radii of the specimen along with the simulated results are displayed in Figs. 16(a and b) for different times. As can be ,seen a major part of the shrinkage takes place in the first couple of hours of the experiment. The simulations are quite accurate, although a small overestimation can be observed in drying shrinkage parallel to the beddings.

A comparison of the numerical and experimental results indicates that the developed transversely isotropic thermoporoelastoplastic model is suitable to predict the drying-induced shrinkage in sedimentary natural clays with anisotropic behavior under transient conditions. The validated model developed in this study can be used to simulate the EDZ. Furthermore, the onset and development of tensile cracks or shear strain localization during the drying of clays, which are two major failure modes in EDZ, can be investigated by coupling either a damage criterion or a regularization method for the post-localization process with the constitutive model developed in this study. However, the latter is beyond the scope of the current study.

The implication of the current THM model is not limited to underground structures. It can also be used to analyze the wetting/drying cycles of shallow subsurface clays under different climatic conditions. Wetting/drying cycles result in swelling/shrinkage of most natural clays, which result in structural damage (e.g., cracks on walls, differential settlement of foundations, etc.). Although the current model was only validated against the drying regime, it can be suitable to simulate the swelling behavior of low to moderate

natural plastic clays and/or modeling wetting and drying cycles in clayey soils (THM behavior of deformable soil) with some modifications.

Conclusion

In this paper, a mathematical framework was laid out to comprehensively study the drying kinetics and drying-induced shrinkage of transversely isotropic Boom clay. A coupled thermo-hydromechanical model was presented in which the evaporation was governed by the equilibrium phase change assumption. The anisotropy of the hydraulic and mechanical features of the Boom clay observed in various prior experiments was incorporated in the hydraulic and mechanical constitutive models. The hydraulic anisotropy was manifested through an intrinsic permeability tensor, and mechanical anisotropy was considered in both elastic and plastic parts of the deformation, while thermal strain was assumed to be isotropic. Following previous studies in the literature, a microstructure secondorder tensor based on the unit normal vector to the bedding planes was employed in the definition of the anisotropic elastic energy function for the elastic model, and in the construction of a projection tensor that incorporates anisotropy effects in the MCC plastic potential function. A non-associative plastic flow rule was assumed based on the experimental observation, and thus an anisotropic yield surface, different from plastic potential, was assumed. Moreover, temperature and suction effects were implemented in the thermoporoelastoplastic constitutive model as isotropic hardening/softening variables. Thermal, hydraulic, and mechanical material parameters in the developed model were

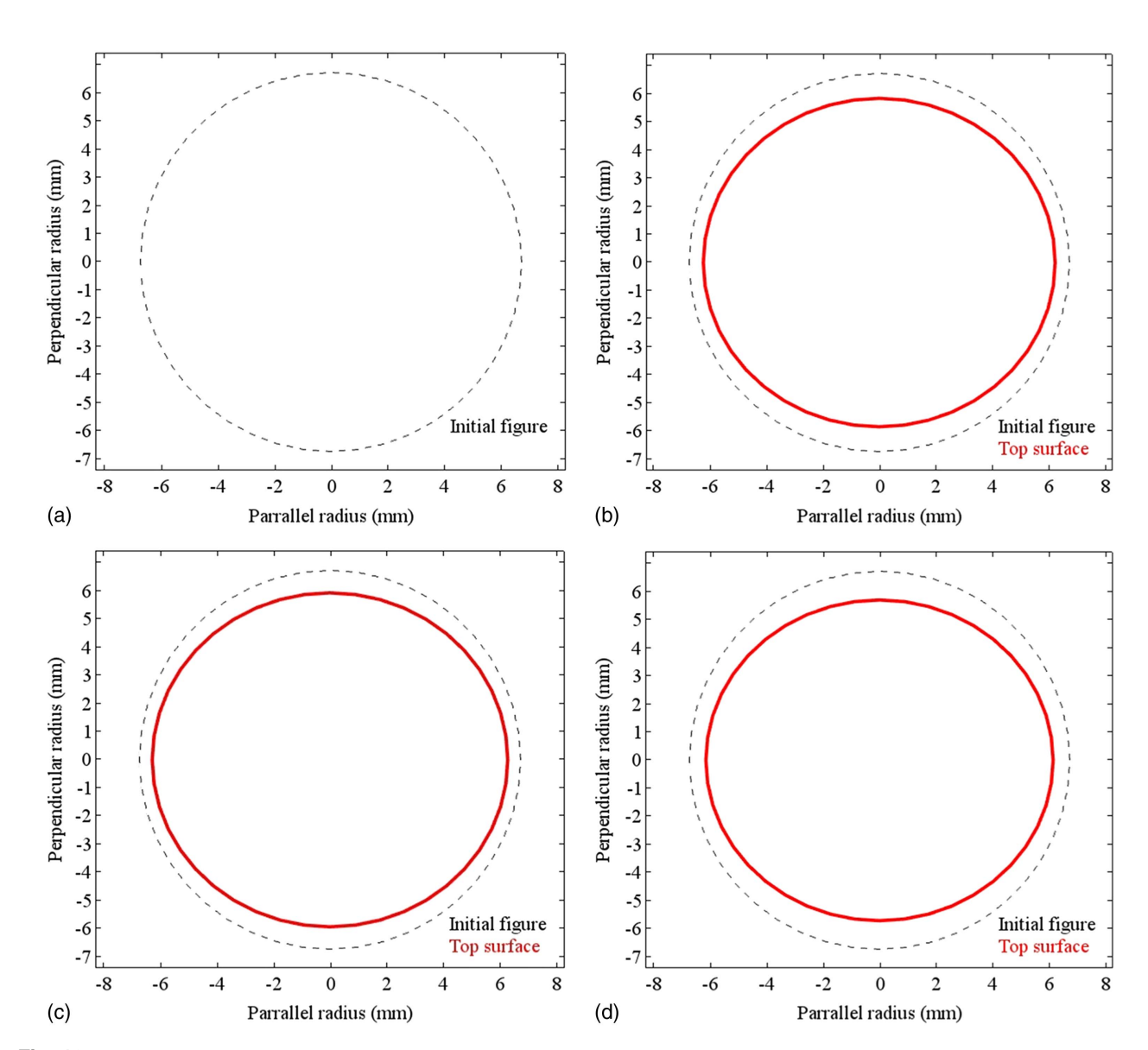


Fig. 13. Variations in the top boundary at different times: (a) initial state; (b) after one hour; (c) after two hours; and (d) after 20 h.

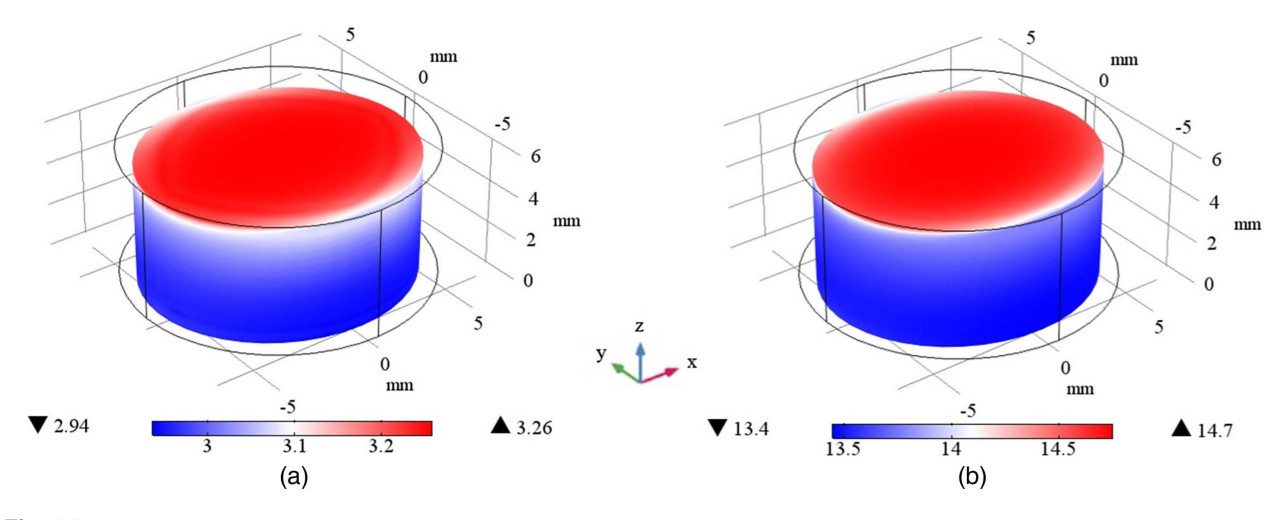


Fig. 14. Volumetric deformation of the sample after 20 h: (a) volumetric elastic strain; and (b) volumetric plastic strain shrinkage.

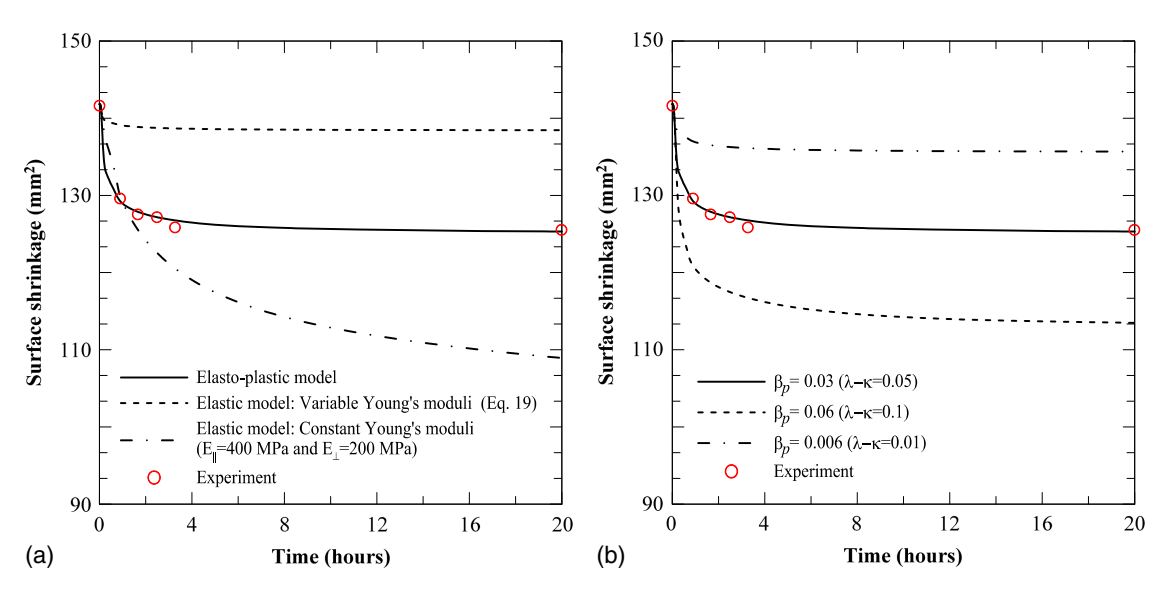


Fig. 15. Sensitivity analysis of the influence of elastic and plastic parameters on the surface shrinkage: (a) Young's moduli; and (b) plastic compressibility modulus.

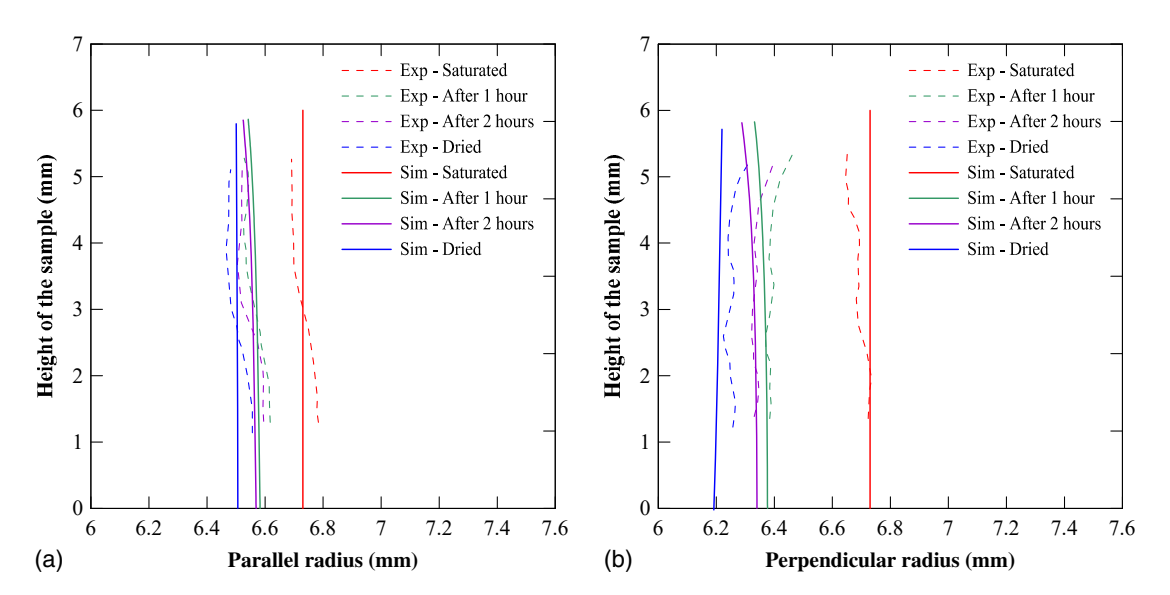


Fig. 16. Comparison of simulated and experimental results for drying-induced shrinkage: Variations of (a) parallel; and (b) perpendicular radii to the bedding planes at different times.

calibrated from the experimental observations on Boom clay and used to simulate the convective drying experiment that was conducted on the same material. The numerical results were compared with the experimental observations on the drying kinetics and drying-induced shrinkage, and reasonable agreement were observed between the experiment and the simulation. Numerical results indicate that during an early stage of evaporation (after one hour of drying) there is a 60% difference in the degree of saturation between the top and bottom surface, because the drying occurs from the top surface. However, after 24 h there are very small changes in the degree of saturation (less than 2%) within the sample. In addition, the results depict a 30% reduction in porosity during the convective drying, while almost 80% of the volume shrinkage is plastic (i.e., irreversible) deformation. Overall, the developed multiphysical model provides an ability to analyze the

THM behavior of unsaturated clays in large-scale modeling with some degree of confidence.

Appendix. Elastic Tangent Tensor

The effective stress and elastic strain in Voigt's notation can be expressed as

$$\mathbf{\sigma}' = \{ \sigma'_{11} \quad \sigma'_{22} \quad \sigma'_{33} \quad \sigma'_{23} \quad \sigma'_{13} \quad \sigma'_{12} \}^T$$
 (36)

$$\mathbf{\varepsilon}^e = \{ \varepsilon_{11}^e \quad \varepsilon_{22}^e \quad \varepsilon_{33}^e \quad \varepsilon_{23}^e \quad \varepsilon_{13}^e \quad \varepsilon_{12}^e \}^T \tag{37}$$

By following the simplified approach proposed by Graham and Houlsby (1983), the transversely isotropic elastic compliance tensor is defined

$$\mathbb{C}^{e} = (\mathbb{D}^{e})^{-1} = E^{*} \times \begin{bmatrix}
1/\alpha_{e}^{2} & -\nu^{*}/\alpha_{e} & -\nu^{*}/\alpha_{e}^{2} & 0 & 0 & 0 \\
-\nu^{*}/\alpha_{e} & 1 & -\nu^{*}/\alpha_{e} & 0 & 0 & 0 \\
-\nu^{*}/\alpha_{e}^{2} & -\nu^{*}/\alpha_{e} & 1/\alpha_{e}^{2} & 0 & 0 & 0 \\
0 & 0 & 0 & (1+\nu^{*})/\alpha_{e} & 0 & 0 \\
0 & 0 & 0 & 0 & (1+\nu^{*})/\alpha_{e}^{2} & 0 \\
0 & 0 & 0 & 0 & 0 & (1+\nu^{*})/\alpha_{e}^{2}
\end{bmatrix}$$
(38)

where $\nu^* = \nu_{||||}$; and $E^* = E_{\perp}$. The compliance tensor in Eq. (38) is defined in a way that the bedding planes are in perpendicular directions. In other words, according to Fig. 1(b), Axes 1 and 3 are parallel to the bedding, and Axis 2 is perpendicular to the bedding planes.

Data Availability Statement

Some or all data, models, or code generated or used during the study are available from the corresponding author by request.

Acknowledgments

The authors would like to gratefully acknowledge the financial support from the National Science Foundation under Grant No. CMMI-1804822.

References

- Aliabadian, Z., G.-F. Zhao, and A. R. Russell. 2019. "Failure, crack initiation and the tensile strength of transversely isotropic rock using the Brazilian test." *Int. J. Rock Mech. Min. Sci.* 122 (Oct): 104073. https://doi.org/10.1016/j.ijrmms.2019.104073.
- Alonso, E., E. Romero, C. Hoffmann, and E. J. E. g. García-Escudero. 2005. "Expansive bentonite-sand mixtures in cyclic controlled-suction drying and wetting." *Eng. Geol.* 81 (3): 213–226.
- Amorosi, A., F. Rollo, and Y. F. Dafalias. 2021. "Relating elastic and plastic fabric anisotropy of clays." *Géotechnique* 71 (7): 1–11. https://doi.org/10.1680/jgeot.19.P.134.
- Baldi, G., T. Hueckel, A. Peano, and R. Pellegrini. 1991. Developments in modelling of thermo-hydro-geomechanical behaviour of Boom clay and clay-based buffer materials. EUR 13365/1. Brussels, Belgium: European Commission.
- Bernier, F., X. L. Li, and W. Bastiaens. 2007. "Twenty-five years' geotechnical observation and testing in the Tertiary Boom Clay formation." *Géotechnique* 57 (2): 229–237. https://doi.org/10.1680/geot.2007.57.2.229.
- Bishop, A. W. 1959. "The principle of effective stress." *Tek. Ukebl.* 39 (9): 859–863.
- Bittelli, M., G. S. Campbell, and F. Tomei. 2015. *Soil physics with Python: Transport in the soil-plant-atmosphere system.* Oxford, UK: Oxford University Press.
- Bittelli, M., F. Ventura, G. S. Campbell, R. L. Snyder, F. Gallegati, and P. R. Pisa. 2008. "Coupling of heat, water vapor, and liquid water fluxes to compute evaporation in bare soils." *J. Hydrol.* 362 (3–4): 191–205. https://doi.org/10.1016/j.jhydrol.2008.08.014.
- Blatz, J. A., Y.-J. Cui, and L. Oldecop. 2008. "Vapour equilibrium and osmotic technique for suction control." *Geotech. Geol. Eng.* 26: 661–673.
- Braun, P., S. Ghabezloo, P. Delage, J. Sulem, and N. Conil. 2021. "Transversely isotropic poroelastic behaviour of the Callovo-Oxfordian claystone: A set of stress-dependent parameters." *Rock Mech. Rock Eng.* 54: 377–396.
- Brutsaert, W. 2005. *Hydrology: An introduction*. Cambridge, UK: Cambridge University Press.

- Brutsaert, W. 2015. "A generalized complementary principle with physical constraints for land-surface evaporation." *Water Resour. Res.* 51 (10): 8087–8093. https://doi.org/10.1002/2015WR017720.
- Bryant, E. C., and W. Sun. 2019. "A micromorphically regularized Camclay model for capturing size-dependent anisotropy of geomaterials." *Comput. Methods Appl. Mech. Eng.* 354 (Sep): 56–95. https://doi.org/10.1016/j.cma.2019.05.003.
- Chapuis, R. P., and M. Aubertin. 2003. "On the use of the Kozeny Carman equation to predict the hydraulic conductivity of soils." *Can. Geotech. J.* 40 (3): 616–628.
- Chaves, E. W. 2013. Notes on continuum mechanics. Berlin: Springer.
- Chen, Y., F. Marinelli, and G. Buscarnera. 2020. "Influence of clay anisotropy on model simulations of wetting collapse." *J. Eng. Mech.* 146 (2): 04019130. https://doi.org/10.1061/(ASCE)EM.1943-7889 0001703
- Cherati, D. Y., and O. Ghasemi-Fare. 2019. "Analyzing transient heat and moisture transport surrounding a heat source in unsaturated porous media using the Green's function." *Geothermics* 81 (Sep): 224–234. https://doi.org/10.1016/j.geothermics.2019.04.012.
- Cherati, D. Y., and O. Ghasemi-Fare. 2021. "Unsaturated thermal consolidation around a heat source." *Comput. Geotech.* 134 (Jun): 104091. https://doi.org/10.1016/j.compgeo.2021.104091.
- Choudhury, B., R. Reginato, and S. Idso. 1986. "An analysis of infrared temperature observations over wheat and calculation of latent heat flux." *Agric. For. Meteorol.* 37 (1): 75–88. https://doi.org/10.1016/0168 -1923(86)90029-8.
- Coccia, C. J. R., and J. S. McCartney. 2016. "Thermal volume change of poorly draining soils I: Critical assessment of volume change mechanisms." *Comput. Geotech.* 80 (Dec): 26–40. https://doi.org/10.1016/j .compgeo.2016.06.009.
- COMSOL. 2018. COMSOL Multiphysics v.5.3a. Stockholm, Sweden: COMSOL.
- Coussy, O. 2004. Poromechanics. New York: Wiley.
- Cui, Y. J., C. Loiseau, and P. Delage. 2002. "Microstructure changes of a confined swelling soil due to suction controlled hydration." In *Proc.*, 3rd Int. Conf. on Unsaturated Soils, UNSAT 2002, 593–598. Berlin: Springer.
- Dafalias, Y. F., M. T. Manzari, and A. G. Papadimitriou. 2006. "SANI-CLAY: Simple anisotropic clay plasticity model." *Int. J. Numer. Anal. Methods Geomech.* 30 (12): 1231–1257. https://doi.org/10.1002/nag.524.
- Delage, P., N. Sultan, and Y. J. Cui. 2000. "On the thermal consolidation of Boom clay." *Can. Geotech. J.* 37 (2): 343–354. https://doi.org/10.1139/t99-105.
- Della Vecchia, G., C. Jommi, A. Lima, and E. Romero. 2010. "Some remarks on the hydro-mechanical modelling of natural and compacted Boom Clay." In *Unsaturated soils*, 1st ed., 803–809. Boca Raton, FL: CRC Press.
- Della Vecchia, G., and E. Romero. 2013. "A fully coupled elastic-plastic hydromechanical model for compacted soils accounting for clay activity." *Int. J. Numer. Anal. Methods Geomech.* 37 (5): 503–535. https:// doi.org/10.1002/nag.1116.

- Dong, Y., N. Lu, and P. J. Fox. 2020. "Drying-induced consolidation in soil." J. Geotech. Geoenviron. Eng. 146 (9): 04020092. https://doi .org/10.1061/(ASCE)GT.1943-5606.0002327.
- François, B., V. Labiouse, A. Dizier, F. Marinelli, R. Charlier, and F. Collin. 2014. "Hollow cylinder tests on Boom Clay: Modelling of strain localization in the anisotropic excavation damaged zone." *Rock Mech. Rock Eng.* 47 (1): 71–86. https://doi.org/10.1007/s00603-012-0348-5.
- François, B., and L. Laloui. 2008. "ACMEG-TS: A constitutive model for unsaturated soils under non-isothermal conditions." *Int. J. Numer. Anal. Methods Geomech.* 32 (16): 1955–1988. https://doi.org/10.1002/nag.712.
- François, B., L. Laloui, and C. Laurent. 2009. "Thermo-hydro-mechanical simulation of ATLAS in situ large scale test in Boom Clay." *Comput. Geotech.* 36 (4): 626–640. https://doi.org/10.1016/j.compgeo.2008.09 .004.
- Gallipoli, D., A. Gens, R. Sharma, and J. Vaunat. 2003. "An elasto-plastic model for unsaturated soil incorporating the effects of suction and degree of saturation on mechanical behavior." *Géotechnique* 53 (1): 123–135. https://doi.org/10.1680/geot.2003.53.1.123.
- Gao, J., J. Deng, K. Lan, Y. Feng, W. Zhang, and H. Wang. 2017. "Porothermoelastic effect on wellbore stability in transversely isotropic medium subjected to local thermal non-equilibrium." *Int. J. Rock Mech. Min. Sci.* 96 (4): 66–84. https://doi.org/10.1016/j.ijrmms.2016.12.007.
- Gens, A., and E. E. Alonso. 1992. "A framework for the behaviour of unsaturated expansive clays." *Can. Geotech. J.* 20 (6). https://doi.org/10 .1139/t92-120.
- Gerard, P., A. Léonard, J.-P. Masekanya, R. Charlier, and F. Collin. 2010. "Study of the soil–atmosphere moisture exchanges through convective drying tests in non-isothermal conditions." *Int. J. Numer. Anal. Methods Geomech.* 34 (12): 1297–1320. https://doi.org/10.1002/nag.866.
- Ghasemi-Fare, O., and P. Basu. 2019. "Coupling heat and buoyant fluid flow for thermal performance assessment of geothermal piles." *Comput. Geotech.* 116 (3): 103211. https://doi.org/10.1016/j.compgeo.2019.103211.
- Ghorbani, A., M. Zamora, and P. Cosenza. 2009. "Effects of desiccation on the elastic wave velocities of clay-rocks." *Int. J. Rock Mech. Min. Sci.* 46 (8): 1267–1272. https://doi.org/10.1016/j.ijrmms.2009.01.009.
- Graham, J., and G. Houlsby. 1983. "Anisotropic elasticity of a natural clay." Géotechnique 33 (2): 165–180. https://doi.org/10.1680/geot.1983.33.2 .165.
- Grant, S. A., and A. Salehzadeh. 1996. "Calculation of temperature effects on wetting coefficients of porous solids and their capillary pressure functions." Water Resour. Res. 32 (2): 261–270. https://doi.org/10 .1029/95WR02915.
- Grzegorz, M., and B. Jacek. 2007. "Non-linear heat and mass transfer during convective drying of kaolin cylinder under non-steady conditions." *Transp. Porous Media* 66 (1): 121–134. https://doi.org/10.1007/s11242 -006-9009-z.
- Guayacan-Carrillo, L.-M., S. Ghabezloo, J. Sulem, D. M. Seyedi, and G. Armand. 2017. "Effect of anisotropy and hydro-mechanical couplings on pore pressure evolution during tunnel excavation in low-permeability ground." *Int. J. Rock Mech. Min. Sci.* 97 (Sep): 1–14.
- Hedan, S., P. Cosenza, V. Valle, P. Dudoignon, A.-L. Fauchille, and J. Cabrera. 2012. "Investigation of the damage induced by desiccation and heating of Tournemire argillite using digital image correlation." Int. J. Rock Mech. Min. Sci. 51 (Apr): 64–75. https://doi.org/10.1016/j.ijrmms.2012.01.001.
- Horseman, S., M. Winter, and D. Enwistle. 1987. Geotechnical characterization of Boom Clay in relation to the disposal of radioactive waste. Brussels, Belgium: European Commission.
- Hubert, J., E. Plougonven, N. Prime, A. Léonard, and F. Collin. 2018. "Comprehensive study of the drying behavior of Boom clay: Experimental investigation and numerical modeling." *Int. J. Numer. Anal. Methods Geomech.* 42 (2): 211–230.
- Jaradat, K. A., and S. L. Abdelaziz. 2020. "Thermomechanical triaxial cell for rate-controlled heating-cooling cycles." *Geotech. Test. J.* 43 (4): 1022–1036. https://doi.org/10.1520/GTJ20180354.
- Jommi, C. 2000. "Remarks on the constitutive modelling of unsaturated soils." In Experimental evidence and theoretical approaches in unsaturated soils, 139–153. London: CRC Press.

- Joshaghani, M., and O. Ghasemi-Fare. 2019. "A Study on thermal consolidation of fine grained soils using modified consolidometer." In *Proc.*, 8th Int. Conf. on Case Histories in Geotechnical Engineering, 148–156. Reston, VA: ASCE.
- Lai, S.-H., J. M. Tiedje, and A. E. Erickson. 1976. "In situ measurement of gas diffusion coefficient in soils." Soil Sci. Soc. Am. J. 40 (1): 3–6.
- Laloui, L., and C. Cekerevac. 2003. "Thermo-plasticity of clays: An isotropic yield mechanism." *Comput. Geotech.* 30 (8): 649–660. https://doi.org/10.1016/j.compgeo.2003.09.001.
- Le, T., P. Delage, Y. Cui, A. Tang, A. Lima, E. Romero, A. Gens, and X. Li. 2008. "Water retention properties of Boom clay: A comparison between different experimental techniques." In *Proc., Unsaturated soils: Advan*ces in geo-Engineering, edited by Toll et al., 229–234. London: Taylor & Francis.
- Lehmann, P., S. Assouline, and D. Or. 2008. "Characteristic lengths affecting evaporative drying of porous media." *Phys. Rev. E* 77 (5): 056309. https://doi.org/10.1103/PhysRevE.77.056309.
- Le Pense, S., C. Arson, and A. Pouya. 2016. "A fully coupled damageplasticity model for unsaturated geomaterials accounting for the ductile–brittle transition in drying clayey soils." *Int. J. Solids Struct.* 91 (Aug): 102–114.
- Li, C., H. Xie, and J. Wang. 2020. "Anisotropic characteristics of crack initiation and crack damage thresholds for shale." *Int. J. Rock Mech. Min. Sci.* 126 (Feb): 104178. https://doi.org/10.1016/j.ijrmms.2019.104178.
- Lima, A. F. A. 2011. Thermo-hydro-mechanical behaviour of two deep Belgium clay formations: Boom and ypresian clays. Barcelona, Spain: Universitat Politècnica de Catalunya.
- Lings, M. L., D. S. Pennington, and D. F. T. Nash. 2000. "Anisotropic stiffness parameters and their measurement in a stiff natural clay." *Géotechnique* 50 (2): 109–125. https://doi.org/10.1680/geot.2000.50.2.109.
- Modaressi, H., and L. Laloui. 1997. "A thermo-viscoplastic constitutive model for clays." Int. J. Numer. Anal. Methods Geomech. 21 (5): 313–335. https://doi.org/10.1002/(SICI)1096-9853(199705)21:5<313:: AID-NAG872>3.0.CO:2-5.
- Mohajerani, M., P. Delage, J. Sulem, M. Monfared, A. M. Tang, and B. Gatmiri. 2012. "A laboratory investigation of thermally induced pore pressures in the Callovo-Oxfordian claystone." *Int. J. Rock Mech. Min. Sci.* 52 (Feb): 112–121. https://doi.org/10.1016/j.ijrmms.2012.02.012.
- Monteith, J., and M. Unsworth. 2013. *Principles of environmental physics:*Plants, animals, and the atmosphere. Cambridge, MA: Academic Press
- Mualem, Y. 1978. "Hydraulic conductivity of unsaturated porous media: Generalized macroscopic approach." *Water Resour. Res.* 14 (2): 325–334. https://doi.org/10.1029/WR014i002p00325.
- Musielak, G., and D. Mierzwa. 2009. "Permanent strains in clay-like material during drying." *Drying Technol.* 27 (7–8): 894–902. https://doi.org/10.1080/07373930903041616.
- Ng, C. W. W., and A. K. Leung. 2012. "Measurements of drying and wetting permeability functions using a new stress-controllable soil column." *J. Geotech. Geoenviron. Eng.* 138 (1): 58–68. https://doi.org/10.1061/(ASCE)GT.1943-5606.0000560.
- Niessner, J., and S. M. Hassanizadeh. 2009. "Modeling kinetic interphase mass transfer for two-phase flow in porous media including fluid–fluid interfacial area." *Transp. Porous Media* 80 (2): 329. https://doi.org/10 .1007/s11242-009-9358-5.
- Nova, R. 1980. "The failure of transversely isotropic rocks in triaxial compression." *Int. J. Rock Mech. Min. Sci. Geomech. Abstr.* 17 (6): 325–332. https://doi.org/10.1016/0148-9062(80)90515-X.
- Novak, M. D. 2010. "Dynamics of the near-surface evaporation zone and corresponding effects on the surface energy balance of a drying bare soil." *Agric. For. Meteorol.* 150 (10): 1358–1365. https://doi.org/10 .1016/j.agrformet.2010.06.005.
- Nuth, M., and L. Laloui. 2008. "Advances in modelling hysteretic water retention curve in deformable soils." *Comput. Geotech.* 35 (6): 835–844. https://doi.org/10.1016/j.compgeo.2008.08.001.
- Or, D., P. Lehmann, E. Shahraeeni, and N. J. V. Shokri. 2013. "Advances in soil evaporation physics—A review." *Vadose Zone J.* 12 (4): 1–16. https://doi.org/10.2136/vzj2012.0163.

- Peron, H., L. Laloui, L.-B. Hu, and T. Hueckel. 2013. "Formation of drying crack patterns in soils: A deterministic approach." *Acta Geotech.* 8 (2): 215–221. https://doi.org/10.1007/s11440-012-0184-5.
- Peron, H., L. Laloui, T. Hueckel, and L. B. Hu. 2009. "Desiccation cracking of soils." Eur. J. Environ. Civ. Eng. 13 (7–8): 869–888. https://doi.org /10.1080/19648189.2009.9693159.
- Philip, J., and D. De Vries. 1957. "Moisture movement in porous materials under temperature gradients." *EOS Trans. Am. Geophys. Union* 38 (2): 222–232. https://doi.org/10.1029/TR038i002p00222.
- Prime, N., S. Levasseur, L. Miny, R. Charlier, A. Léonard, and F. J. C. Collin. 2015. "Drying-induced shrinkage of Boom clay: An experimental investigation." *Can. Geotech. J.* 53 (3): 396–409.
- Romero, E., G. Della Vecchia, and C. Jommi. 2011. "An insight into the water retention properties of compacted clayey soils." *Géotechnique* 61 (4): 313–328. https://doi.org/10.1680/geot.2011.61.4.313.
- Romero, E., A. Gens, and A. Lloret. 1999. "Water permeability, water retention and microstructure of unsaturated compacted Boom clay." Eng. Geol. 54 (1–2): 117–127. https://doi.org/10.1016/S0013-7952 (99)00067-8.
- Romero, E., and C. Jommi. 2008. "An insight into the role of hydraulic history on the volume changes of anisotropic clayey soils." Water Resour. Res. 44 (5): W12412. https://doi.org/10.1029/2007WR006558.
- Rutqvist, J., L. Börgesson, M. Chijimatsu, A. Kobayashi, L. Jing, T. S. Nguyen, J. Noorishad, and C. F. Tsang. 2001. "Thermohydromechanics of partially saturated geological media: Governing equations and formulation of four finite element models." *Int. J. Rock Mech. Min. Sci.* 38 (1): 105–127. https://doi.org/10.1016/S1365-1609(00)00068-X.
- Saito, H., J. Šimůnek, and B. P. Mohanty. 2006. "Numerical analysis of coupled water, vapor, and heat transport in the Vadose zone." *Vadose Zone J.* 5 (2): 784–800. https://doi.org/10.2136/vzj2006.0007.
- Sánchez, M., A. Gens, L. do Nascimento Guimarães, and S. Olivella. 2005. "A double structure generalized plasticity model for expansive materials." *Int. J. Numer. Anal. Methods Geomech.* 29 (8): 751–787. https://doi.org/10.1002/nag.434.
- Sánchez, M., A. Gens, and S. Olivella. 2012. "THM analysis of a large-scale heating test incorporating material fabric changes." *Int. J. Numer. Anal. Methods Geomech.* 36 (4): 391–421. https://doi.org/10.1002/nag.1011
- Sánchez, M., A. Gens, M. V. Villar, and S. Olivella. 2016. "Fully coupled thermo-hydro-mechanical double-porosity formulation for unsaturated soils." *Int. J. Geomech.* 16 (6): D4016015. https://doi.org/10.1061 /(ASCE)GM.1943-5622.0000728.
- Sánchez, M., O. L. Manzoli, and L. J. Guimarães. 2014. "Modeling 3-D desiccation soil crack networks using a mesh fragmentation technique." Comput. Geotech. 62 (Oct): 27–39. https://doi.org/10.1016/j.compgeo.2014.06.009.
- Semnani, S. J., J. A. White, and R. I. Borja. 2016. "Thermoplasticity and strain localization in transversely isotropic materials based on anisotropic critical state plasticity." *Int. J. Numer. Anal. Methods Geomech.* 40 (18): 2423–2449. https://doi.org/10.1002/nag.2536.
- Shahraeeni, E., P. Lehmann, and D. Or. 2012. "Coupling of evaporative fluxes from drying porous surfaces with air boundary layer: Characteristics of evaporation from discrete pores." Water Resour. Res. 48 (9): 12. https://doi.org/10.1029/2012WR011857.
- Shokri, N., P. Lehmann, and D. Or. 2009. "Critical evaluation of enhancement factors for vapor transport through unsaturated porous media." Water Resour. Res. 45 (10): W10433. https://doi.org/10.1029/2009 WR007769.
- Sitarenios, P., and M. Kavvadas. 2020. "A plasticity constitutive model for unsaturated, anisotropic, nonexpansive soils." *Int. J. Numer. Anal. Meth-ods Geomech.* 44 (4): 435–454. https://doi.org/10.1002/nag.3028.
- Smits, K. M., A. Cihan, T. Sakaki, and T. H. Illangasekare. 2011. "Evaporation from soils under thermal boundary conditions: Experimental and modeling investigation to compare equilibrium-and nonequilibrium-based approaches." Water Resour. Res. 47 (5): W05540. https://doi.org/10.1029/2010WR009533.
- Spencer, A. J. M. 1984. Continuum theory of the mechanics of fibre-reinforced composites. Berlin: Springer.

- Sultan, N., Y.-J. Cui, and P. Delage. 2010. "Yielding and plastic behaviour of Boom clay." *Géotechnique* 60 (9): 657–666. https://doi.org/10.1680/geot.7.00142
- Sviercoski, R., Y. Efendiev, and B. Mohanty. 2018. "Upscaling the coupled water and heat transport in the shallow subsurface." *Water Resour. Res.* 54 (2): 995–1012. https://doi.org/10.1002/2017WR021490.
- Tamizdoust, M. M., and O. Ghasemi-Fare. 2020a. "Comparison of thermoporoelastic and thermo-poroelastoplastic constitutive models to analyze THM process in clays." In *Proc.*, 2nd Int. Conf. on Energy Geotechnics and E3S Web of Conf., 04008. Les Ulis, France: EDP Sciences.
- Tamizdoust, M. M., and O. Ghasemi-Fare. 2020b. "A fully coupled thermoporo-mechanical finite element analysis to predict the thermal pressurization and thermally induced pore fluid flow in soil media." *Comput. Geotech.* 117 (Jan): 103250. https://doi.org/10.1016/j.compgeo.2019.103250.
- Tamizdoust, M. M., and O. Ghasemi-Fare. 2020c. "Utilization of nonequilibrium phase change approach to analyze the nonisothermal multiphase flow in shallow subsurface soils." *Water Resour. Res.* 56 (10): e2020WR027381. https://doi.org/10.1029/2020WR027381.
- Tamizdoust, M. M., and O. Ghasemi-Fare. 2022. "Long-term thermohydraulic response of the shallow subsurface soil in the vicinity of a buried horizontal heat source." *Int. J. Heat Mass Transfer* 183 (Feb): 122120.
- Tamizdoust, M. M., A. Moradi, and O. Ghasemi-Fare. 2020. "Numerical analysis of variation of saturation and moisture transport at the vicinity of a heat source." In *Proc.*, *Geo-Congress* 2020: Geo-Systems, Sustainability, Geoenvironmental Engineering, and Unsaturated Soil Mechanics, 349–357. Reston, VA: ASCE.
- Tang, A.-M., and Y.-J. Cui. 2005. "Controlling suction by the vapour equilibrium technique at different temperatures and its application in determining the water retention properties of MX80 clay." Can. Geotech. J. 42 (1): 287–296. https://doi.org/10.1139/t04-082.
- Tarantino, A. 2009. "A water retention model for deformable soils." *Géotechnique* 59 (9): 751–762. https://doi.org/10.1680/geot.7.00118.
- Terzaghi, K. 1925. "Principles of soil mechanics I—Phenomena of cohesion of clays." *Eng. News-Rec.* 95 (19): 742–746.
- Trautz, A. C., K. M. Smits, and A. Cihan. 2015. "Continuum-scale investigation of evaporation from bare soil under different boundary and initial conditions: An evaluation of nonequilibrium phase change." Water Resour. Res. 51 (9): 7630–7648. https://doi.org/10.1002/2014 WR016504.
- Tsang, C. F., J. D. Barnichon, J. Birkholzer, X. L. Li, H. H. Liu, and X. Sillen. 2012. "Coupled thermo-hydro-mechanical processes in the near field of a high-level radioactive waste repository in clay formations." *Int. J. Rock Mech. Min. Sci.* 49 (Jan): 31–44. https://doi.org/10.1016/j.ijrmms.2011.09.015.
- Vahedifard, F., T. D. Cao, S. K. Thota, and E. Ghazanfari. 2018. "Nonisothermal models for soil–water retention curve." J. Geotech. Geoenviron. Eng. 144 (9): 04018061. https://doi.org/10.1061/(ASCE)GT.1943-5606.0001939.
- Vanderborght, J., T. Fetzer, K. Mosthaf, K. M. Smits, and R. Helmig. 2017. "Heat and water transport in soils and across the soil-atmosphere interface: 1. Theory and different model concepts." Water Resour. Res. 53 (2): 1057–1079. https://doi.org/10.1002/2016WR019982.
- van Genuchten, M. T. 1980. "A closed-form equation for predicting the hydraulic conductivity of unsaturated soils." *Soil Sci. Soc. Am. J.* 44 (5): 892–898. https://doi.org/10.2136/sssaj1980.03615995004400050002x.
- Vecchia, G. D., and E. Romero. 2013. "A fully coupled elastic-plastic hydromechanical model for compacted soils accounting for clay activity." Int. J. Numer. Anal. Methods Geomech. 37 (5): 503–535. https:// doi.org/10.1002/nag.1116.
- Veiskarami, M., and M. M. Tamizdoust. 2017. "Bifurcation analysis in sands under true triaxial conditions with coaxial and noncoaxial plastic flow rules." J. Eng. Mech. 143 (10): 04017120. https://doi.org/10.1061 /(ASCE)EM.1943-7889.0001344.
- Venda Oliveira, P. J., and L. J. Lemos. 2014. "Experimental study of isotropic and anisotropic constitutive models." J. Geotech. Geoenviron. Eng. 140 (8): 06014008. https://doi.org/10.1061/(ASCE)GT.1943-5606.0001141.

- Vesga, L. 2008. "Equivalent effective stress and compressibility of unsaturated kaolinite clay subjected to drying." J. Geotech. Geoenviron. Eng. 134 (3): 366–378. https://doi.org/10.1061/(ASCE)1090-0241(2008) 134:3(366).
- Villar, M. V., P. L. Martín, F. J. Romero, R. J. Iglesias, and V. Gutiérrez-Rodrigo. 2016. "Saturation of barrier materials under thermal gradient." Geomech. Energy Environ. 8 (Dec): 38–51. https://doi.org/10.1016/j.gete.2016.05.004.
- Viola, R., M. Tuller, D. Or, and J. Drasdis. 2005. "Microstructure of claysand mixtures at different hydration states." In *Proc.*, *Int. Symp. on Ad*vanced Experimental Unsaturated Soil Mechanics, 437–442. London: Taylor, Francis Group.
- Volckaert, G., L. D. C. Ortiz, M. Put, S. T. Horseman, J. F. Harrington, V. Fioravante, and M. D. Impey. 1995. MEGAS: Modelling and experiments on gas migration in repository host rocks. Final Rep.—Phase 1, CEC Nuclear Science and Technology Series, European commission Rep., EUR 16235-EN. Brussels, Belgium: European Commission.
- Wang, C., and P. J. Fox. 2020. "Numerical model for heat transfer in saturated layered soil with effective porosity." J. Geotech. Geoenviron. Eng. 146 (12): 04020135. https://doi.org/10.1061/(ASCE)GT.1943-5606.0002390.
- Wheeler, S., R. Sharma, and M. Buisson. 2003. "Coupling of hydraulic hysteresis and stress–strain behaviour in unsaturated soils." *Géotechnique* 53 (1): 41–54. https://doi.org/10.1680/geot.2003.53.1.41.
- Wilson, G., D. Fredlund, and S. Barbour. 1997. "The effect of soil suction on evaporative fluxes from soil surfaces." Can. Geotech. J. 34 (1): 145–155. https://doi.org/10.1139/t96-078.

- Wilson, G. W., D. Fredlund, and S. Barbour. 1994. "Coupled soil-atmosphere modelling for soil evaporation." *Can. Geotech. J.* 31 (2): 151–161. https://doi.org/10.1139/t94-021.
- Yang, D. S., M. Bornert, S. Chanchole, H. Gharbi, P. Valli, and B. Gatmiri. 2012. "Dependence of elastic properties of argillaceous rocks on moisture content investigated with optical full-field strain measurement techniques." *Int. J. Rock Mech. Min. Sci.* 53 (Jul): 45–55. https://doi.org/10 .1016/j.ijrmms.2012.04.004.
- Yu, H., W. Chen, Z. Gong, Y. Ma, G. Chen, and X. Li. 2018. "Influence of temperature on the hydro-mechanical behavior of Boom Clay." *Int. J. Rock Mech. Min. Sci.* 108 (Apr): 189–197. https://doi.org/10.1016/j.ijrmms.2018.04.023.
- Zamanian, S. 2016. Probabilistic performance assessment of deteriorating buried concrete sewer pipes. Columbus, OH: Ohio State Univ.
- Zamanian, S., J. Hur, and A. Shafieezadeh. 2020. "A high-fidelity computational investigation of buried concrete sewer pipes exposed to truckloads and corrosion deterioration." *Eng. Struct.* 221 (Oct): 111043. https://doi.org/10.1016/j.engstruct.2020.111043.
- Zhang, Z. F. 2011. "Soil water retention and relative permeability for conditions from oven-dry to full saturation." *Vadose Zone J.* 10 (4): 1299–1308. https://doi.org/10.2136/vzj2011.0019.
- Zhao, Y., and R. I. Borja. 2020. "A continuum framework for coupled solid deformation—fluid flow through anisotropic elastoplastic porous media." *Comput. Methods Appl. Mech. Eng.* 369 (Sep): 113225. https://doi.org/10.1016/j.cma.2020.113225.
- Zhao, Y., S. J. Semnani, Q. Yin, and R. I. Borja. 2018. "On the strength of transversely isotropic rocks." *Int. J. Numer. Anal. Methods Geomech.* 42 (16): 1917–1934. https://doi.org/10.1002/nag.2809.